Available online at www.sciencedirect.com
SCIENCE DIRECT®
Journal of Computational Physics 212 (2006) 400–435
JOURNAL OF COMPUTATIONAL PHYSICS
www.elsevier.com/locate/jcp

# Scale-separating operators for variational multiscale large eddy simulation of turbulent flows

Volker Gravemeier *

*Center for Turbulence Research, Stanford University, Stanford, CA 94305, USA*

Received 3 November 2004; received in revised form 6 July 2005; accepted 7 July 2005
Available online 24 August 2005

**Abstract**

A general class of scale-separating operators based on combined multigrid operators is proposed and analyzed in this work. The operators of this class are designed for variational multiscale large eddy simulation using a finite volume or finite element method. Two representatives are compared to discrete smooth filters, which are widely used in the traditional large eddy simulation literature; the comparison shows that they are not only theoretically different, but also yield considerable differences in the respective numerical results. Dynamic as well as constant-coefficient-based subgrid-scale modeling is used within the multiscale environment. All of the scale-separating operators are implemented in a second-order accurate energy-conserving finite volume method and tested for the case of a turbulent channel flow. One operator shows particularly remarkable results in the framework of the variational multiscale large eddy simulation, that is, profiles are obtained for velocity and kinetic energy which are considerably closer to the respective profiles from a direct numerical simulation than are the profiles resulting from the application of the other operators considered in the present study. Furthermore, this particular operator proves to be very efficient with regard to the important aspect of computational cost, that is, a reduction in computing time ranging from about 25% up to about 150% compared to the other operators. The introduction of a substantial amount of subgrid viscosity to the small scales, particularly in the buffer layer of the channel, appears to be crucial for the good results achieved with this method.


*Keywords:* Turbulence; Large eddy simulation; Variational multiscale method; Scale separation; Subgrid-scale modeling

* Present address: Technical University of Munich, Boltzmannstr. 15, D-85747 Garching, Germany. Tel.: +1 49 89 28915245; fax: +1 49 89 28915301.
*E-mail address:* vgravem@lnm.mw.tum.de.

0021-9991/$ - see front matter 
doi:10.1016/j.jcp.2005.07.007

## 1. Introduction

Large eddy simulation (LES) is widely considered to be a promising approach for the numerical simulation of turbulent flows. Although the computational effort usually required for LES is considerably less than the one for a direct numerical simulation (DNS), in which scales of the order of magnitude of the smallest length scale, the Kolmogorov scale, are resolved (see [47]), it is still of substantial complexity. LES aims at a complete resolution of only the large-scale structure of the turbulent flow. The effect on the large scales of the smaller scales, which are not acquired by this resolution, is modeled. Thus, a basic ingredient of the approach consists of the separation of resolved and unresolved scales. General overviews of the classical LES procedure may, for instance, be found in [53] or [54]. Some recent advances for LES in complex geometries are reported in [46].

The variational multiscale method was established as a theoretical framework in [24] and further developed for general problems in computational mechanics in [25]. The basic concept involves separating the problem scales into a predefined number of scale groups. This theoretical framework was also applied to the problem of the incompressible Navier–Stokes equations in [26], in order to facilitate LES of turbulent flows. The initial concept of the variational multiscale method, as Hughes and co-workers proposed it in their publications, assumes a separation of two scale ranges. Nevertheless, the framework allows various other arrangements going beyond this two-scale decomposition. In [4,14], the variational multiscale method for LES has recently been broadened by raising the number of separated scale ranges beyond the original twofold separation. A completely different numerical treatment for any of these ranges is enabled. Such a three-scale separation accounts specifically for large resolved scales, small resolved scales, and unresolved scales.

Apart from the initial separation and potentially different treatment of the respective scale ranges, two important aspects characterize the variational multiscale LES. Firstly, a variational projection separates scale ranges within the variational multiscale method rather than a spatial filter in the traditional LES. Secondly, the (direct) influence of the subgrid-scale model is confined to the small resolved scales. Thus, the large resolved scales are solved as a DNS (i.e., without any (direct) influence of the modeling term). Of course, the large resolved scales are still influenced indirectly by the subgrid-scale model due to the inherent coupling of all scales. A new residual-based variant of the variational multiscale LES which retracts this second aspect has recently been developed in [2].

At this stage, it should be pointed out that the variational multiscale method is essentially a theoretical framework for the separation of scales. Corresponding practical implementations within the variational multiscale framework are still rare. For such practical methods, it is crucial that a clear separation of the different scale ranges is actually achieved. The scale-separating approach developed in the present study is implemented into the CDP-$\alpha$ code, the flagship LES code of the Center for Turbulence Research. It is the recently redesigned and rewritten version of the original CDP code [52] (named after the late Charles David Pierce, 1969–2002). Underlying the code is a colocated finite volume method particularly suited for applications on unstructured grids. Within this computational environment, the separation of scales is developed in this work.

In the traditional LES, the theoretical way of identifying the resolved part of the velocity $\boldsymbol{u}^{\mathrm{res}}$ consists of applying a spatial filter $G$ to the unknown velocity $\boldsymbol{u}$ in the domain $\Omega$, resulting in

$$\boldsymbol{u}^{\mathrm{res}}(\boldsymbol{x},t) = \int_{\Omega} G(\boldsymbol{x}-\xi)\boldsymbol{u}(\xi,t)\,\mathrm{d}\xi. \tag{1}$$

This procedure was first proposed in [39]. In practice, however, most of the numerical simulations performed in physical space do not rely on a spatial filtering process like (1), unless the so-called "pre-filtering technique" is used, see [54]. Rather, the resolution of the underlying numerical discretization is used to define the resolved part of the velocity $\boldsymbol{u}^h$, with the superscript $h$ indicating the characteristic length scale

of the discretization. Nevertheless, the application of a spatial filter in the sense of (1) may become necessary, for instance, for separating the resolved scales into large and small resolved scales in the context of a dynamic modeling procedure. This produces a large-scale velocity $\overline{\boldsymbol{u}}^h$.

The three most commonly used filters for LES are the box filter, the Gaussian filter, and the sharp or spectral cutoff filter. It is referred to [54] for a discussion of these filters. Of these, only the sharp cutoff filter has the property of a projector for the multiple application of the operator, that is,

$$\hat{G}^n = \hat{G} \circ \hat{G} \circ \cdots \circ \hat{G} = \hat{G}, \quad n > 1. \tag{2}$$

Applications of the variational multiscale method for LES in spectral space, such as, e.g., [27,28], were executed in a straightforward manner using the sharp cutoff filter.

In physical space applications, the situation becomes much more complicated. Discrete filters with compact support are usually applied. They may be identified as discrete approximations of the filter $G$ in (1) (i.e., as discrete approximations of the box filter or the Gaussian filter in physical space), see [55]. All those filters commute with differentiation, a prerequisite for the formulation of the filtered Navier–Stokes equations, in *homogeneous* cases, see [54]. However, problems occur both for the continuous filter itself and the discrete approximation when using homogeneous filters for *inhomogeneous* cases, for instance, as soon as a domain boundary is approached. The need for the filtering to be commutative with differentiation also in inhomogeneous cases was emphasized in [13]. Moreover, second-order commuting continuous filters were developed to address this problem. In [62], this strategy was extended to higher-order commuting filters as well as discrete approximations of the continuous filters.

Some applications of the variational multiscale method were accomplished without relying on a variational projection as the scale-separating operation (i.e., merely applying the subgrid-scale model to the small resolved scales). The filtering analog of the variational multiscale method provides the framework in this case, see [63]. For the actual simulations, a discrete approximation of a top-hat filter based on the trapezoidal rule was applied in [33] as well as [63], and good results were obtained. These findings raise questions concerning the importance of the actual scale-separating operators used as well as the necessity for this operator to be a projector. The present study addresses these questions.

As aforementioned, it is intended to implement all scale-separating operators into the existing hybrid unstructured finite volume code CDP-$\alpha$. In the context of discrete filters, this requires representations suited for unstructured grids. Commutative discrete filters for unstructured grids were developed in [44], using the work of [62] as a starting point. Subsequently, a new construction procedure based on least-squares techniques was presented in [21]. Filters for unstructured cases based on the numerical solution of high-order elliptic problems were proposed in [49]. For finite element methods, in particular, a number of discrete filters suited for application on unstructured grids were described in [31]. One of them, a node-oriented discrete version of a box filter, was then further investigated in [58,59] on structured finite element grids.

In this work, unstructured analogs of the discrete filters based on the trapezoidal rule as well as on Simpson's rule are used. The results achieved with these discrete filters are compared to the results obtained with the general class of scale-separating operators, based on combined multigrid operators in a two-grid procedure,which are proposed in this work. In contrast to the unstructured analogs of the discrete filters, the representatives of this class of scale-separating operators are equally suited for the application within both a finite volume method and a finite element method. One particular representative of this class indeed has the property of a projector. A projector of this type was also addressed in [37] as well as [64]. In [37], it was used for a combined finite element/volume method on the basis of a cell-agglomeration procedure.

Beyond the scale-separating operators mentioned above, there exist other ways to achieve a separation of scales. In [32], a hierarchical-based continuous Galerkin finite element method was used, which had previously been developed in [66]. Here, shape functions up to a certain polynomial degree $p$ represent the large scales, and the remaining shape functions up to the level of resolution are supposed to capture the smaller scales. In a discontinuous Galerkin method, this may be done in a similar way, see [5]. In the classical

notion of finite element methods, such methods may be denoted as "$p$-type" scale separations (i.e., based on the polynomial degree of the approximation), in contrast to "$h$-type" scale separations based on the discretization characterized by the length scale $h$.

A completely different way to address the problem was shown in [16,17]. The equation system consisting of the equation related to the large scales (i.e., the large-scale equation) and the equation related to the small scales (i.e., the small-scale equation) was, in fact, handled as a pair of coupled non-linear variational equations. This is in compliance with the original perception in [26], where the large- and the small-scale part of the solution is expected to be obtained by solving those coupled non-linear equations. In the implementable approach in [16,17], the large- and small-scale equations were independently solved in an iterative procedure, updating the dependencies of the respective equation on the other scales. Furthermore, a localized approach was chosen on the small-scale level. As a result, this approach is, on the one hand, very efficient from the computational point of view. On the other hand, however, it substantially limits the potential amount of small scales captured due to the neglect of non-local interdependencies within the small scales.

The proposed methods of this work are applied to the case of a turbulent channel flow. A large number of numerical realizations of turbulent flow in a channel already exist. The results from a DNS for flows at three different Reynolds numbers

$$Re_\tau = \frac{u_\tau \delta_c}{\nu}$$

up to 590 were reported in [48], where $u_\tau$,$\delta_c$, and $\nu$ denote the turbulent wall-shear velocity, the channel half-width, and the kinematic viscosity, respectively. The data from that report will be used as reference data in the present work, where flows at Reynolds numbers 180 and 590 will be investigated. Turbulent channel flow also served as one of the first test cases for the variational multiscale LES in [28]. That study was later complemented by Oberai and Hughes [50], reporting the case $Re_\tau = 590$. Another study in this respect was [33], comparing the subgrid-scale modeling approach of the variational multiscale method with other modeling approaches in the context of turbulent channel flow.

All of the aforementioned studies have one important aspect in common: the use of a spectral method with higher-order accuracy in the homogeneous $x_1$–$x_3$-planes of the channel. In this work, the method applied is of second-order accuracy overall, without any special treatment for the homogeneous planes within the channel. With regard to future applications in more complex geometries, performance of the variational multiscale LES within such a numerical environment is the more relevant test case, since spectral methods are by no means suited to such applications. The introduction of a generally larger numerical error due to the use of a second-order accurate method, combined with a relatively coarse resolution, was investigated in [38] at a high-Reynolds-number channel flow ($Re_\tau \approx 1000$). Similar evaluations were reported in [56] for a flow at an even higher Reynolds number $Re_\tau \approx 1800$ as well as in [61] for flows at the Reynolds numbers $Re_\tau = 180$ and $Re_\tau = 590$.

This work basically follows the general guideline expressed in the idea that there exists an inherent link between, on the one hand, *physically motivated turbulence modeling* and, on the other hand, *numerically motivated modeling to account for inevitable errors due to an inadequate resolution*. A combined strategy relying on this observation has already been pointed out as a very promising tool in [4,14]. Another recent approach appearing to step in the same direction is the work in [36]. Initial considerations of this approach seem to establish this method as a counterpart of the variational multiscale method within a finite difference method (D. Carati, B. Knaepen, personal communication).

The rest of this paper is organized as follows. In Section 2, the variational formulation for a separation of three scales, namely large resolved, small resolved, and unresolved scales, is introduced. The various scale-separating operators are presented and analyzed in Section 3. Additionally, the specific treatment of Dirichlet boundaries is addressed and the characteristic length-scale ratio of the operators is identified preliminarily. In Section 4, subgrid-scale modeling within the variational multiscale LES is addressed. Some

aspects of the implementation in the CDP-$\alpha$ code are mentioned in Section 5, followed by the description of the numerical simulations of turbulent channel flow in Section 6. Section 7 contains conclusions of this study.

## 2. Variational three-scale formulation

The set of incompressible Navier–Stokes equations is given as

$$\frac{\partial \boldsymbol{u}}{\partial t} + \nabla \cdot (\boldsymbol{u} \otimes \boldsymbol{u}) + \nabla p - 2\nu \nabla \cdot \boldsymbol{\varepsilon}(\boldsymbol{u}) = \boldsymbol{f} \quad \text{in } \Omega \times (0,T), \tag{3}$$

$$\nabla \cdot \boldsymbol{u} = 0 \quad \text{in } \Omega \times (0,T), \tag{4}$$

where $\boldsymbol{u}$ denotes the velocity vector, $p$ the kinematic pressure (i.e., pressure divided by density), $\nu$ the kinematic viscosity, which is assumed to be constant, $\boldsymbol{\varepsilon}(\boldsymbol{u})$ the rate-of-deformation tensor, defined as the symmetric part of the spatial gradient of the velocity subject to

$$\boldsymbol{\varepsilon}(\boldsymbol{u}) = \tfrac{1}{2}\left[\nabla \boldsymbol{u} + (\nabla \boldsymbol{u})^{\mathrm{T}}\right],$$

$\boldsymbol{f}$ the body force vector, $\Omega$ the spatial domain with domain boundary $\Gamma$, and $T$ the simulation time. Furthermore, a Dirichlet boundary condition

$$\boldsymbol{u} = \boldsymbol{g} \quad \text{on } \Gamma \times (0,T), \tag{5}$$

where the domain boundary $\Gamma$ is assumed to be a pure Dirichlet boundary, and an initial condition

$$\boldsymbol{u} = \boldsymbol{u}_0 \quad \text{in } \Omega \times \{0\},$$

where the initial velocity field $\boldsymbol{u}_0$ is assumed to be divergence-free, are defined. Aside from Dirichlet boundary conditions, only periodic boundary conditions are used in the numerical example at the end of the present study. Thus, Neumann boundary conditions are omitted here, although they would basically pose no additional problem for the developments of this work.

A weighted residual formulation of the Navier–Stokes equations is given as follows: find $\{\boldsymbol{u}, p\} \in \mathscr{S}_{\boldsymbol{u}p}$, such that

$$B_{\mathrm{NS}}(\boldsymbol{v}, q; \boldsymbol{u}, p) = (\boldsymbol{v}, \boldsymbol{f})_{\Omega} \quad \forall \{\boldsymbol{v}, q\} \in \mathscr{V}_{\boldsymbol{u}p}, \tag{6}$$

where $\boldsymbol{v}$ and $q$ denote the weighting functions. $\mathscr{S}_{\boldsymbol{u}p}$ and $\mathscr{V}_{\boldsymbol{u}p}$ represent the combined form of the solution and weighting function spaces, respectively, for velocity and pressure in the sense that $\mathscr{S}_{\boldsymbol{u}p} := \mathscr{S}_{\boldsymbol{u}} \times \mathscr{S}_p$ and $\mathscr{V}_{\boldsymbol{u}p} := \mathscr{V}_{\boldsymbol{u}} \times \mathscr{V}_p$. The $L_2$-inner product in the domain $\Omega$ on the right-hand side of (6) is defined as usual:

$$(\boldsymbol{v}, \boldsymbol{f})_{\Omega} = \int_{\Omega} \boldsymbol{v} \cdot \boldsymbol{f} \; \mathrm{d}\Omega. \tag{7}$$

Using the notation in (7), the form $B_{\mathrm{NS}}(\boldsymbol{v}, q; \boldsymbol{u}, p)$ on the left-hand side of (6), which is linear on the first slot (i.e., $\boldsymbol{v}, q$) and non-linear on the second slot (i.e., $\boldsymbol{u}, p$), is defined as

$$B_{\mathrm{NS}}(\boldsymbol{v}, q; \boldsymbol{u}, p) = \left(\boldsymbol{v}, \frac{\partial u}{\partial t}\right)_{\Omega} + (\boldsymbol{v}, \nabla \cdot (\boldsymbol{u} \otimes \boldsymbol{u}))_{\Omega} + (\boldsymbol{v}, \nabla p)_{\Omega} - (\boldsymbol{v}, 2\nu \nabla \cdot \boldsymbol{\varepsilon}(\boldsymbol{u}))_{\Omega} + (q, \nabla \cdot \boldsymbol{u})_{\Omega}. \tag{8}$$

The scales of the problem are now separated into three scale ranges, as proposed in [4,14]: large resolved scales, small resolved scales, and unresolved scales. In terms of the underlying weighting and solution function spaces $\mathscr{V}_{\boldsymbol{u}p}$ and $\mathscr{S}_{\boldsymbol{u}p}$, this scale separation yields

$$\mathscr{V}_{up} = \overline{\mathscr{V}}_{up} \oplus \mathscr{V}'_{up} \oplus \hat{\mathscr{V}}_{up},$$
$$\mathscr{S}_{up} = \overline{\mathscr{S}}_{up} \oplus \mathscr{S}'_{up} \oplus \hat{\mathscr{S}}_{up}.$$

According to this, the weighting functions read

$$\boldsymbol{v} = \overline{\boldsymbol{v}} + \boldsymbol{v}' + \hat{\boldsymbol{v}}, \quad q = \overline{q} + q' + \hat{q}$$

and, analogously, the solution functions are composed as

$$\boldsymbol{u} = \overline{\boldsymbol{u}} + \boldsymbol{u}' + \hat{\boldsymbol{u}}, \quad p = \overline{p} + p' + \hat{p}.$$

Since it is linear in the weighting functions $\boldsymbol{v}$ and $q$, Eq. (6) may now be decomposed into a system of three equations as

$$B_{\mathrm{NS}}(\overline{\boldsymbol{v}}, \overline{q}; \overline{\boldsymbol{u}} + \boldsymbol{u}' + \hat{\boldsymbol{u}}, \overline{p} + p' + \hat{p}) = (\overline{\boldsymbol{v}}, \boldsymbol{f})_{\Omega} \quad \forall \{\overline{\boldsymbol{v}}, \overline{q}\} \in \overline{\mathscr{V}}_{up}, \tag{9}$$
$$B_{\mathrm{NS}}(\boldsymbol{v}', q'; \overline{\boldsymbol{u}} + \boldsymbol{u}' + \hat{\boldsymbol{u}}, \overline{p} + p' + \hat{p}) = (\boldsymbol{v}', \boldsymbol{f})_{\Omega} \quad \forall \{\boldsymbol{v}', q'\} \in \mathscr{V}'_{up}, \tag{10}$$
$$B_{\mathrm{NS}}(\hat{\boldsymbol{v}}, \hat{q}; \overline{\boldsymbol{u}} + \boldsymbol{u}' + \hat{\boldsymbol{u}}, \overline{p} + p' + \hat{p}) = (\hat{\boldsymbol{v}}, \boldsymbol{f})_{\Omega} \quad \forall \{\hat{\boldsymbol{v}}, \hat{q}\} \in \hat{\mathscr{V}}_{up}, \tag{11}$$

It is assumed that

$$B_{\mathrm{NS}}(\overline{\boldsymbol{v}}, \overline{q}; \hat{\boldsymbol{u}}, \hat{p}) + (\overline{\boldsymbol{v}}, \nabla \cdot ((\overline{\boldsymbol{u}} + \boldsymbol{u}') \otimes \hat{\boldsymbol{u}} + \hat{\boldsymbol{u}} \otimes (\overline{\boldsymbol{u}} + \boldsymbol{u}')))_{\Omega} \approx 0, \tag{12}$$

relying on a clear separation of the large-scale space and the space of unresolved scales. Note that assumption (12) is the same as assuming locality of interactions in Fourier space. As a result, the large-scale equation (9) may be simplified to

$$B_{\mathrm{NS}}(\overline{\boldsymbol{v}}, \overline{q}; \overline{\boldsymbol{u}} + \boldsymbol{u}', \overline{p} + p') = (\overline{\boldsymbol{v}}, \boldsymbol{f})_{\Omega} \quad \forall \{\overline{\boldsymbol{v}}, \overline{q}\} \in \overline{\mathscr{V}}_{up}. \tag{13}$$

It is not intended to explicitly resolve any quantities which are termed "unresolved" a priori. Thus, Eq. (11) for the unresolved scales is not solved. Taking into account the effect of the unresolved scales onto the small scales is the only desire. Several approaches lend themselves to this purpose (see [14]), but the focus here is on the subgrid viscosity concept as a usual and well-established way of taking into account the effect of unresolved scales in the traditional LES. The small-scale equation (10) then reads

$$B_{\mathrm{NS}}(\boldsymbol{v}', q'; \overline{\boldsymbol{u}} + \boldsymbol{u}', \overline{p} + p') - \left(\boldsymbol{v}', \nabla \cdot \left(2\nu'_{\mathrm{T}} \boldsymbol{\varepsilon}(\boldsymbol{u}')\right)\right)_{\Omega} = (\boldsymbol{v}', \boldsymbol{f})_{\Omega} \quad \forall \{\boldsymbol{v}', q'\} \in \mathscr{V}_{up}. \tag{14}$$

Due to assumption (12), the subgrid viscosity term directly acts only on the small resolved scales. Indirect influence on the large resolved scales, however, is ensured due to the coupling of the large- and the small-scale equations. Appropriate modeling approaches for the subgrid viscosity $\nu'_{\mathrm{T}}$, where the prime indicates the relation to the small resolved scales, will be discussed in Section 4. Note that the reason for introducing a model term in the present formulation is mathematically slightly different from the usual necessity of introducing a model term due to the appearance of a subgrid-scale stress tensor in the strong formulation of the Navier–Stokes equations in a classical LES. Nevertheless, the physical necessity of accounting for the missing effect of unresolved scales onto the resolved scales is the same in both cases.

The weighted residual equations above may serve as the starting point for either a finite element formulation or a finite volume formulation. The inherent link between these two numerical methods is pointed out, for instance, in [29]. A particular finite element method based on the combined system consisting of the large- and small-scale equations (13) and (14) may be found in [16,17].

The focus here is on the finite volume method. The presupposition for the application of the finite volume method is a discretization of the domain $\Omega$ into $n_{\mathrm{cv}}$ control volumes $\Omega_i$ ($i = 1, \ldots, n_{\mathrm{cv}}$), with control volume boundaries $\Gamma_i$. The weighting functions are chosen to be

$$\boldsymbol{v}^h = \sum_i \boldsymbol{v}_i^h, \quad q^h = \sum_i q_i^h,$$

where

$$\boldsymbol{v}_i^h = \mathbf{1}, \qquad q_i^h = 1 \quad \text{in } \Omega_i \tag{15}$$

and zero elsewhere. In (15), $\mathbf{1}$ explicitly means that each component of $\boldsymbol{v}_i^h$ is of unit value. The characteristic control volume length of the discretization is $h$. With these definitions at hand, the weighted residual equation (6) may be reformulated as a variational finite volume equation for each $\boldsymbol{v}_i^h$ and $q_i^h$: find $\{\boldsymbol{u}^h, p^h\} \in \mathscr{S}_{\boldsymbol{up}}^h$, such that

$$B_{\mathrm{NS}}^{\mathrm{FV}}(\boldsymbol{v}_i^h, q_i^h; \boldsymbol{u}^h, p^h) = (\boldsymbol{v}_i^h, \boldsymbol{f})_{\Omega}. \tag{16}$$

The term on the right-hand side of (16) may be defined analogously to (7) as

$$(\boldsymbol{v}, \boldsymbol{f})_{\Gamma_i} = \int_{\Gamma_i} \boldsymbol{v} \cdot \boldsymbol{f} \; \mathrm{d}\Gamma,$$

where $\Gamma_i$ denotes the boundary of the support of $\boldsymbol{v}_i^h$ and $q_i^h$, respectively. Furthermore, the semi-linear form $B_{\mathrm{NS}}^{\mathrm{FV}}(\boldsymbol{v}_i^h, q_i^h; \boldsymbol{u}^h, p^h)$ on the left-hand side of (16) is obtained from (8) after applying Gauss' theorem to the convective term, the pressure term, the viscous term, and the continuity term as

$$B_{\mathrm{NS}}^{\mathrm{FV}}(\boldsymbol{v}_i^h, q_i^h; \boldsymbol{u}^h, p^h) = \left(\boldsymbol{v}_i^h, \frac{\partial \boldsymbol{u}^h}{\partial t}\right)_{\Omega} + (\boldsymbol{v}_i^h, (\boldsymbol{u}^h \otimes \boldsymbol{u}^h) \cdot \boldsymbol{n})_{\Gamma_i} + (\boldsymbol{v}_i^h, p^h \cdot \boldsymbol{n})_{\Gamma_i} - (\boldsymbol{v}_i^h, \nu(\nabla \boldsymbol{u}^h) \cdot \boldsymbol{n})_{\Gamma_i} + (q_i^h, \boldsymbol{u}^h \cdot \boldsymbol{n})_{\Gamma_i}. \tag{17}$$

In (17), $\boldsymbol{n}$ indicates the respective outward normal vector of unit length to $\Gamma_i$. Note the change of the viscous term from the stress-divergence form in the weighted residual formulation in (8) to the conventional form for the finite volume formulation in (17). This change may already be carried out here in view of the actual implementation, where the divergence of the velocity will be monitored to remain as close to zero as possible throughout the simulation and, thus, the fulfillment of the continuity equation will be approximately achieved in the discrete case. The same change will be carried out for the subgrid viscosity term below. Further information on the monitoring of the discrete fulfillment of the continuity equation will be provided in Section 5.

The scale separation to be presented in Section 3 relies on a level of complete resolution, which is indicated by the characteristic control volume length $h$. In terms of the velocity, this reads

$$\boldsymbol{u}^h = (\boldsymbol{u} + \boldsymbol{u}')^h.$$

With respect to this complete resolution level, a large-scale resolution level is identified a priori. This level is characterized by the control volume length $\overline{h}$, where $\overline{h} > h$, and, accordingly, yields a large-scale velocity $\overline{\boldsymbol{u}}^{\overline{h}}$. The small-scale velocity is consistently defined on the complete resolution level, characterized by the length $h$, as

$$\boldsymbol{u}'^h = \boldsymbol{u}^h - \overline{\boldsymbol{u}}^h, \tag{18}$$

where $\overline{\boldsymbol{u}}^h$ is the large-scale value transferred to this level. The large-scale weighting function is defined as

$$\overline{\boldsymbol{v}}^{\overline{h}} = \sum_i \overline{\boldsymbol{v}}_i^{\overline{h}},$$

where

$$\overline{\boldsymbol{v}}_i^{\overline{h}} = \mathbf{1} \quad \text{in } \overline{\Omega}_i$$

and zero elsewhere. $\overline{\Omega}_i$ denotes the $i$th control volume of the discretization with the characteristic control volume length $\overline{h}$. The large-scale equation (13) and the small-scale equation (14) with the subgrid viscosity term are now reunified on the basis of the preceding finite volume formulation. The unified equation may be written in compact form with the help of (18) for each $\boldsymbol{v}_i^h$, $q_i^h$, and $\overline{\boldsymbol{v}}_i^{\overline{h}}$, where the control volume $\Omega_i$ on the

complete resolution level is contained in the control volume $\overline{\Omega}_i$ on the large-scale resolution level: find $\{\boldsymbol{u}^h, p^h\} \in \mathscr{S}^h_{\boldsymbol{up}}$, such that

$$\begin{aligned} & B^{\mathrm{FV}}_{\mathrm{NS}}(\boldsymbol{v}^h_i, q^h_i; \boldsymbol{u}^h, p^h) - \left(\boldsymbol{v}'^h_i, \nu'_{\mathrm{T}}(\nabla \boldsymbol{u}'^h) \cdot \boldsymbol{n}\right)_{\Gamma'_i} \\ & = B^{\mathrm{FV}}_{\mathrm{NS}}(\boldsymbol{v}^h_i, q^h_i; \boldsymbol{u}^h, p^h) - \left(\boldsymbol{v}^h_i, \nu'_{\mathrm{T}}\left(\nabla\left(\boldsymbol{u}^h - \overline{\boldsymbol{u}}^h\right)\right) \cdot \boldsymbol{n}\right)_{\Gamma_i} + \left(\overline{\boldsymbol{v}}^h_i, \nu'_{\mathrm{T}}\left(\nabla\left(\boldsymbol{u}^h - \overline{\boldsymbol{u}}^h\right)\right) \cdot \boldsymbol{n}\right)_{\overline{\Gamma}_i} \\ & = B^{\mathrm{FV}}_{\mathrm{NS}}(\boldsymbol{v}^h_i, q^h_i; \boldsymbol{u}^h, p^h) - \left(\boldsymbol{v}^h_i, \nu'_{\mathrm{T}}\left(\left(\nabla \boldsymbol{u}^h\right) \cdot \boldsymbol{n} - \left(\nabla \overline{\boldsymbol{u}}^h\right) \cdot \boldsymbol{n}\right)\right)_{\Gamma_i} + \left(\overline{\boldsymbol{v}}^h_i, \nu'_{\mathrm{T}}\left(\left(\nabla \boldsymbol{u}^h\right) \cdot \boldsymbol{n} - \left(\nabla \overline{\boldsymbol{u}}^h\right) \cdot \boldsymbol{n}\right)\right)_{\overline{\Gamma}_i} \\ & = (\boldsymbol{v}^h_i, \boldsymbol{f})_{\Omega}, \end{aligned} \tag{19}$$

where the boundary $\Gamma_i$ is split up into a large-scale boundary $\overline{\Gamma}_i$ and, accordingly, a small-scale boundary subject to

$$\Gamma'_i = \Gamma_i - \overline{\Gamma}_i. \tag{20}$$

The commutation between differentiation and the definition of the large scales in terms of a projection ensuring the equality of the second and the third line in (19) remains to be proven. A proof in this regard may be found in [34] in the context of a finite element formulation for a viscous term integrated by parts and defined on the domain $\Omega_i$ rather than the boundary $\Gamma_i$. However, that proof may be transferred to this case in a straightforward manner. The inherent scale separation remains obvious in (19) merely due to the subgrid viscosity term.

## 3. Separation of scales

The scale-separating transformation is generally formulated as

$$\overline{\boldsymbol{u}}^h = S\left[\boldsymbol{u}^h\right], \tag{21}$$

where $S$ denotes the scale-separating operator acting on a finite-dimensional velocity field $\boldsymbol{u}^h$ and yielding a finite-dimensional large-scale velocity field $\overline{\boldsymbol{u}}^h$.

### 3.1. Discrete smooth filters for scale separation

Discrete filters based on weighted averages with compact support are usually applied in practical LES. The two most prominent representatives are obtained by applying either the trapezoidal rule or Simpson's rule. In [55], it was shown that discrete filters may be constructed in two steps. Firstly, the continuous convolution filter in (1) is approximated by a truncated Taylor series expansion in the sense of a continuous differential operator. Secondly, this continuous differential operator is discretized to obtain a discrete form of the operator. In order to compute the large-scale part $\overline{u}^h_i$ of a piecewise linear scalar function $u^h$ in the control volume $\Omega_i$ as part of a uniform 1-D discretization, this is given as

$$\overline{u}^h_i = \tfrac{1}{4}(u^h_{i-1} + 2u^h_i + u^h_{i+1})$$

for the trapezoidal rule and

$$\overline{u}^h_i = \tfrac{1}{6}(u^h_{i-1} + 4u^h_i + u^h_{i+1})$$

for Simpson's rule. In the three-dimensional case, a discrete filter for a structured grid of hexahedra may be constructed in two ways: either by linear combination or by product. Following the strategy of construction by linear combination, we may finally end up with the face-based filter described in [31]. However, it is well known that filters constructed by linear combination are less sensitive to the cross modes than the ones

constructed by product, see [54]. Due to this, construction by product is used throughout this work. Following the rules for construction by product in [55], the large-scale velocity vector in the center of $\Omega_i$ is obtained as

$$\overline{\boldsymbol{u}}_i^h = \frac{1}{8}\boldsymbol{u}_i^h + \frac{1}{16}\sum_{f=1}^{n_{\mathrm{fpcv}}}\boldsymbol{u}_f^h + \frac{1}{32}\sum_{e=1}^{n_{\mathrm{epcv}}}\boldsymbol{u}_e^h + \frac{1}{64}\sum_{n=1}^{n_{\mathrm{npcv}}}\boldsymbol{u}_n^h \tag{22}$$

for the trapezoidal filter and

$$\overline{\boldsymbol{u}}_i^h = \frac{8}{27}\boldsymbol{u}_i^h + \frac{2}{27}\sum_{f=1}^{n_{\mathrm{fpcv}}}\boldsymbol{u}_f^h + \frac{1}{54}\sum_{e=1}^{n_{\mathrm{epcv}}}\boldsymbol{u}_e^h + \frac{1}{216}\sum_{n=1}^{n_{\mathrm{npcv}}}\boldsymbol{u}_n^h \tag{23}$$

for Simpson's filter, with the number of faces $n_{\mathrm{fpcv}}$, edges $n_{\mathrm{epcv}}$, and nodes $n_{\mathrm{npcv}}$ per control volume being 6, 12, and 8, respectively. $u_f^h$, $u_e^h$, and $u_n^h$ denote the velocity vectors at the center of control volumes sharing at most one face, one edge, and one node with $\Omega_i$, respectively.

In the unstructured case, a two-step procedure for constructing the filters is performed, with the goal of reproducing formulas (22) and (23) in the structured case. For the trapezoidal filter, a volume-weighted averaging procedure at every node including all control volumes $\Omega_i$ attached to this node is performed subject to

$$\overline{\boldsymbol{u}}_n^h = \frac{\sum_{i\in I_n}|\Omega_i|\boldsymbol{u}_i^h}{\sum_{i\in I_n}|\Omega_i|}, \tag{24}$$

with $I_n$ denoting the index set containing all control volumes $i$ attached to node $n$. As a result, a large-scale velocity $\overline{\boldsymbol{u}}_n^h$ at node $n$ is obtained. It should be noted that, for unstructured grids with abrupt variations of volume measures within small distances, it may be advisable to use a simple non-volume-weighted average instead of (24). Afterwards, the large-scale velocity at the center of the control volume is collected as the averaged value, calculated by including all nodes of this control volume according to

$$\overline{\boldsymbol{u}}_i^h = \frac{1}{n_{\mathrm{npcv}}}\sum_{n\in N_i}\overline{\boldsymbol{u}}_n^h, \tag{25}$$

where $N_i$ denotes the index set containing all nodes $n$ of the control volume $i$. A filter created by this two-step procedure was used in [22]. It may be verified by the reader that the formula in (22) can be recovered for the structured case by removing the volume weighting in (24). The unstructured trapezoidal filter defined by (24) and (25) is labeled $S^{\mathrm{tf}}$.

An unstructured analog of Simpson's filter is more involved in that it uses an edge- as well as a face-based data transfer, in addition to the node-based transfer for the trapezoidal filter. The volume-weighted averaging at edges and faces reads

$$\overline{\boldsymbol{u}}_e^h = \frac{\sum_{l\in L_e}|\Omega_l|\boldsymbol{u}_l^h}{\sum_{l\in L_e}|\Omega_l|}, \quad \overline{\boldsymbol{u}}_f^h = \frac{\sum_{m\in M_f}|\Omega_m|\boldsymbol{u}_m^h}{\sum_{m\in M_f}|\Omega_m|}, \tag{26}$$

with $L_e$ and $M_f$ denoting the index sets containing all control volumes attached to the interiors of edge $e$ and face $f$, respectively. The node-, edge-, and face-based values in (24) and (26) are now collected in an averaged sense, including the actual value in the control volume. The large-scale velocity at the center of the control volume is then obtained as

$$\overline{\boldsymbol{u}}_i^h = \frac{1}{n_{\mathrm{npcv}} + n_{\mathrm{epcv}} + n_{\mathrm{fpcv}} + 1}\left[\sum_{n\in N_i}\overline{\boldsymbol{u}}_n^h + \sum_{e\in E_i}\overline{\boldsymbol{u}}_e^h + \sum_{f\in F_i}\overline{\boldsymbol{u}}_f^h + \boldsymbol{u}_i^h\right], \tag{27}$$

where $E_i$ and $F_i$ denote the index sets containing all edges $e$ and all faces $f$ of the control volume $i$. Again, it may be verified by the reader that the formula in (23) can be recovered for the structured case by removing the volume weighting in (24) and (26). The unstructured version of Simpson's filter defined by (24), (26), and (27) is labeled $S^{\mathrm{sf}}$.

### 3.2. Combined multigrid operators for scale separation

As a geometrical basis for the present approach, two grids are created: a coarser grid, which is called the "parent" grid, and a finer grid, which is called the "child" grid. The child grid is obtained by an isotropic hierarchical subdivision of the parent grid, similar to the procedure described in [45]. In contrast to a usual parent–child relationship in multigrid solvers, where the parent needs to know only the number of its children, a complete parent–child knowledge base is set up here (i.e., every parent knows about every child and vice versa). More details concerning the implementation will be given in Section 5.

**Remarks**

1. Hybrid unstructured grids may contain tetrahedra, hexahedra, prisms, and pyramids. However, only two different types of faces, namely triangles and quadrangles, occur for these four different types of control volumes. Based on the fact that a factor of two is most often used in a dynamic modeling procedure for the relation of the cutoff length scale for the large resolved scales to the one for all resolved scales, an initial subdivision procedure using this factor is chosen. Both a parent triangular face and a parent quadrangular face subdivided isotropically result in four child faces of the same type. For the actual 3-D control volumes, isotropic subdivision of either a parent tetrahedron or hexahedron, for example, results in eight children. A parent hexahedron along with its eight child hexahedra is depicted in Fig. 1. Illustrations of subdivided tetrahedra, prisms, and pyramids may be found in [45]. Obviously, this kind of refinement is not restricted to a subdivision by factor 2. Other integer factors (e.g., 3 or 4) may be applied and result in considerably lower ratios of the spaces containing the large resolved scales to the spaces containing the small resolved scales.
2. Several references concerning multigrid methods in general may be found in the literature. An introductory work with particular emphasis on applications in computational fluid dynamics is, for instance, [65]. In particular, Chapter 5 of [65] deals with the topics of restriction and prolongation. Some sections in [10] are also devoted to multigrid methods in the context of computational fluid dynamics.

The general class of scale-separating operators based on multigrid operators is defined as

$$\overline{\boldsymbol{u}}^h = S^{\mathrm{m}}[\boldsymbol{u}^h] = P \circ R[\boldsymbol{u}^h] = P[\overline{\boldsymbol{u}}^{\bar{h}}], \tag{28}$$

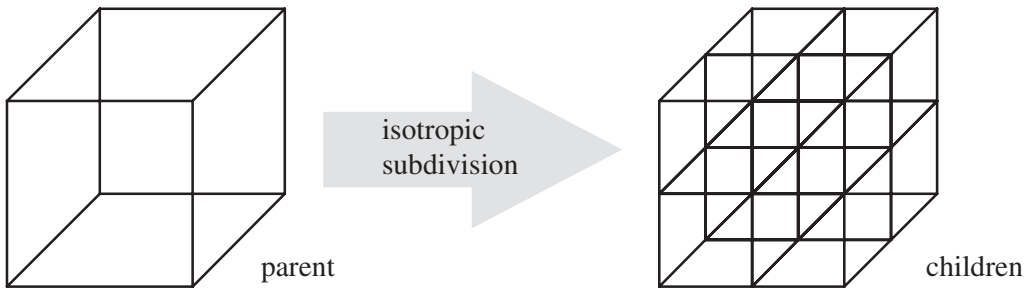


Fig. 1. Parent hexahedron with eight child hexahedra.

where the scale-separating operator $S^m$ consists of the sequential application of a restriction operator $R$ and a prolongation operator $P$. Applying the restriction operator on $\boldsymbol{u}^h$ yields a large-scale velocity $\overline{\boldsymbol{u}}^{\bar{h}}$ defined at the degrees of freedom of the parent grid, which is then prolongated, in order to obtain a large-scale velocity $\overline{\boldsymbol{u}}^h$ defined at the degrees of freedom of the child grid. Various restriction as well as prolongation operators may be used in (28).

Here, however, the attention is focused on two special combinations of restriction and prolongation operators. Both of them rely on the same restriction operator, but apply different prolongation operators afterwards. The restriction operator is defined to be a volume-weighted average over all the child control volumes within one parent control volume subject to

$$\overline{\boldsymbol{u}}_j^{\bar{h}} = \frac{\sum_{i\in\overline{N}_j}|\Omega_i|\boldsymbol{u}_i^h}{\sum_{i\in\overline{N}_j}|\Omega_i|}, \tag{29}$$

where $\overline{\boldsymbol{u}}_j^{\bar{h}}$ denotes the large-scale velocity at the center of the parent control volume $\overline{\Omega}_j$ and $\overline{N}_j$ the index set containing all child control volumes in $\overline{\Omega}_j$. The first prolongation operator $P^{\mathrm{p}}$ yields a constant prolongation as

$$\overline{\boldsymbol{u}}_i^h = P^{\mathrm{p}}\left[\overline{\boldsymbol{u}}_j^{\bar{h}}\right]_i = \overline{\boldsymbol{u}}_j^{\bar{h}} \quad \forall\Omega_i \subset \overline{\Omega}_j \tag{30}$$

and zero elsewhere. The scale-separating operator defined as

$$S^{\mathrm{pm}} := P^{\mathrm{p}} \circ R \tag{31}$$

has the property of a projector, indicated by the additional superscript "p". A scale-separating projection such as (31) is already well-known in the context of wavelets (see, e.g., [6] for a general overview). For structured grids, the restriction operator $R$ defined in (29) is exactly the Haar-basis low-pass transform and the prolongation operator $P^{\mathrm{p}}$ defined in (30) is exactly the Haar-basis low-pass adjoint transform. More general projections for applications on unstructured grids may be found in [1,7]. Besides the special case (31) considered here, any scale-separating operator $S^{\mathrm{m}} := P \circ R$ represents a projection with respect to the child grid, whenever $P \circ R = I$ on the parent grid.

The second prolongation operator considered in this work yields a linear prolongation subject to

$$\overline{\boldsymbol{u}}_i^h = P^{\mathrm{s}}\left[\overline{\boldsymbol{u}}_j^{\bar{h}}\right]_i = \overline{\boldsymbol{u}}_j^{\bar{h}} + \left(\nabla^{\bar{h}}\overline{\boldsymbol{u}}_j^{\bar{h}}\right)\cdot\left(\boldsymbol{r}_i - \overline{\boldsymbol{r}}_j\right) \quad \forall\Omega_i \subset \overline{\Omega}_j \tag{32}$$

and zero elsewhere. The vectors $\boldsymbol{r}_i$ and $\boldsymbol{r}_j$ denote geometrical vectors pointing to the centers of the child control volume $\Omega_i$ and the parent control volume $\overline{\Omega}_j$, respectively. The discrete gradient operator $\nabla^{\bar{h}}$ on the parent grid is here defined, e.g., for the application on the velocity vector $\overline{\boldsymbol{u}}_j^{\bar{h}}$ at the center of the parent control volume $\overline{\Omega}_j$ as

$$\nabla^{\bar{h}}\overline{\boldsymbol{u}}_j^{\bar{h}} = \sum_{n\in\overline{V}_j}\overline{\boldsymbol{w}}_n^j \otimes \left(\overline{\boldsymbol{u}}_n^{\bar{h}} - \overline{\boldsymbol{u}}_j^{\bar{h}}\right), \tag{33}$$

where $\overline{V}_j$ denotes the index set containing all neighbouring parent control volumes $n$ of the parent control volume $j$. The vectorial geometrical weighting parameter $\overline{\boldsymbol{w}}_n^j$ depends on a measure of the parent control volume $\overline{\Omega}_j$, a measure of the respective neighbouring parent control volume $\overline{\Omega}_n$, and the difference between $\overline{\boldsymbol{r}}_j$ and the geometrical vector pointing to the center of $\overline{\Omega}_n$ (i.e., $\overline{\boldsymbol{w}}_n^j = \overline{\boldsymbol{w}}_n^j\left(|\overline{\Omega}_j|, |\overline{\Omega}_n|, \overline{\boldsymbol{r}}_n - \overline{\boldsymbol{r}}_j\right)$). The geometrical weighting parameter $\overline{\boldsymbol{w}}_n^j$ is constructed by a least-squares procedure in the present case. Alternatives for the calculation of the discrete gradient operator (e.g., using Gauss' theorem) are conceivable, see [10].

Due to the linear prolongation, values from neighbouring parent control volumes and, consequently, child control volumes contained in these neighbouring parent control volumes influence the final large-scale value in the child control volume $\Omega_i$. The prolongation $P^{\mathrm{s}}$ does not provide us with a projective scale-separating

operation. It rather produces a smoothing prolongation, which is, at least, smoother than the prolongation produced by $P^{\mathrm{p}}$. Thus, it is indicated by the additional superscript "s" and the complete scale-separating operator is defined as

$$S^{\mathrm{sm}} := P^{\mathrm{s}} \circ R.$$

The fact that $S^{\mathrm{sm}}$ is not a projector, in contrast to $S^{\mathrm{pm}}$, is easily shown already for a simple model problem on a uniform 1-D discretization, see Fig. 2. Being a projector refers to the basic requirement that a multiple application of the scale-separating operator is equal to a single application, which has already been stated for the sharp cutoff filter in spectral space in (2). In Fig. 2, $S^{\mathrm{pm}}$ and $S^{\mathrm{sm}}$ are applied twice to a 1-D curve. For $S^{\mathrm{pm}}$, the large-scale value at the center of a parent control volume, obtained as a result of the restriction (29), is injected to all child control volumes of this parent control volume according to (30), see the middle part of Fig. 2(a). The same curve is achieved for the repeated application of $S^{\mathrm{pm}}$, see the lower part of Fig. 2(b). Already for this simple 1-D model problem, it can be shown that $S^{\mathrm{sm}}$ does not share the projective property due to the inequality of the curves in the middle and the lower part of Fig. 2(b). Of course, the same may be inferred for the unstructured 3-D case. The dashed line in Fig. 2(b) indicates the linear interpolation of the large-scale values at the centers of the parent control volumes, which are obtained as a result of the restriction (29). Fig. 2(b) shows that, in contrast to the situation in Fig. 2(a), the left and right neighbour parent control volumes have to be taken into account to determine the values in the child control volumes of the depicted parent control volumes 1–3.

Alternative definitions for the restriction as well as the prolongation operator are certainly conceivable. For example, differential operators with additional volume weighting on non-uniform grids were used in [61] to define the restriction and prolongation operators for those author's multilevel algorithm. However, their specific choice for the parameters within the differential operators extended the scope of the operators even beyond the nearest neighbour of a coarse grid control volume. This is due to the fact that, on the one hand, their restriction operator took into account fine-grid control volumes located in neighbouring coarse-grid control volumes and, on the other hand, their prolongation operator, similar to $P^{\mathrm{s}}$, was influenced by neighbouring coarse-grid control volumes. At boundaries, in particular, such an extended range of influence

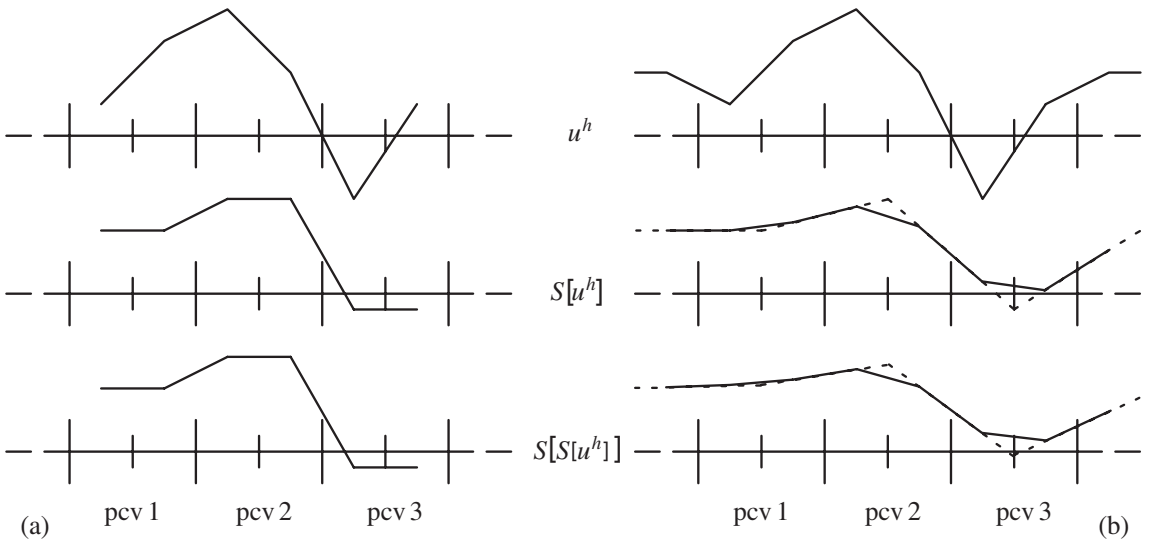


Fig. 2. Applying the multigrid scale-separating operators twice for a 1-D model problem: (a) pm; (b) sm (dashed line indicates linear interpolation of the large-scale values at the parent control volume centers).

including child control volumes within the next to nearest neighbour parent control volume might lead to substantial problems in the context of an implementation such as the one which will be described in the subsequent section.

With regard to the overall strategy in, e.g., [61], it should be emphasized that it is not intended to perform an actual solution step on the parent grid based on the restriction operator used in the present study, although the choice of combined multigrid operators as scale-separating operators basically opens up this opportunity. In this work, the focus is on the influence of the scale separation on the quality of the results (i.e., *accuracy* is the main goal of this work). In a subsequent study, the attention may be shifted to the potential gain in computational *efficiency* due to the exploitation of the parent grid (or further, even coarser grids) for an actual solution strategy in the sense of a multigrid solver.

It will now be briefly shown that $S^{\mathrm{pm}}$, besides being a projector, represents a self-adjoint operator. In [64], the adjoint filter of a general continuous filter, later specialized to a continuous kernel filter in the sense of (1), and the adjoint filter of a general discrete filter were determined. Here, this procedure is transferred to the case of a scale-separating operator acting on a discrete field subject to (21). At first, two important conditions are addressed. The normalization condition requires a discrete constant field to remain unaltered by the scale-separating operation subject to

$$S[c^h] = c^h, \tag{34}$$

where $c^h = 1$ throughout the domain $\Omega$. It may be verified by the reader that (34) is satisfied for all operators defined in Sections 3.1 and 3.2. The conservation condition requires the discrete integral of an arbitrary function $f^h$ over the domain $\Omega$ to remain unaltered by the application of the scale-separating operator in the sense that

$$\sum_i S[f^h]_i |\Omega_i| = \sum_i f_i^h |\Omega_i|, \quad i = 1, \ldots, n_{\mathrm{cv}}. \tag{35}$$

It is referred to [64] for a discussion of the implications of the conservation condition.

The adjoint scale-separating operator $S_{\mathrm{a}}$ corresponding to $S$ is defined in a discrete sense as

$$\sum_i S_{\mathrm{a}}[f^h]_i g_i^h |\Omega_i| = \sum_i f_i^h S[g^h]_i |\Omega_i|, \quad i = 1, \ldots, n_{\mathrm{cv}}, \tag{36}$$

for two arbitrary discrete functions $f^h$ and $g^h$. It can be proven that a scale-separating operator satisfying the normalization condition (34) corresponds to an adjoint scale-separating operator fulfilling the conservation condition (35):

$$\sum_i S_{\mathrm{a}}[f^h]_i |\Omega_i| = \sum_i S_{\mathrm{a}}[f^h]_i c_i^h |\Omega_i| = \sum_i f_i^h S[c^h]_i |\Omega_i| = \sum_i f_i^h c_i^h |\Omega_i| = \sum_i f_i^h |\Omega_i|.$$

This leads to the conclusion that a self-adjoint scale-separating operator (i.e., an operator for which $S = S_{\mathrm{a}}$) also represents a conservative operator, if $S$ satisfies (34). Nevertheless, it should be emphasized that the converse is not true (i.e., a normalized and conservative scale-separating operator does not necessarily imply that this operator is self-adjoint), see [64].

If the scale-separating operator in control volume $\Omega_i$ is now defined by way of its underlying matrix $A_{ij}$ subject to

$$S[f^h]_i = \sum_{j \in \mathrm{NH}} A_{ij} |\Omega_j| f_j \quad \forall i \in \mathrm{NH}, \tag{37}$$

the adjoint scale-separating operator may then easily be obtained based on the transpose of the matrix as

$$S_{\mathrm{a}}[f^h]_i = \sum_{j \in \mathrm{NH}} A_{ji} |\Omega_j| f_j \quad \forall i \in \mathrm{NH}. \tag{38}$$

In (37) and (38), NH denotes the geometrical "neighbourhood" of control volume $\Omega_i$ containing all control volumes $\Omega_j$ contributing to the calculation of the large-scale value in $\Omega_i$. For $S^{\mathrm{tf}}$ and $S^{\mathrm{sf}}$, NH is defined to contain all control volumes $\Omega_j$ sharing at least one node with $\Omega_i$. For $S^{\mathrm{pm}}$, NH contains all remaining child control volumes within the same parent control volume. Additionally, all child control volumes in parent control volumes sharing a face with the actual parent control volume are also included in the definition of NH for $S^{\mathrm{sm}}$. By inserting (37) and (38) in the definition of the adjoint operator (36), the reader may verify the correctness of (38). It may be stated that a self-adjoint scale-separating operator necessarily requires its underlying matrix to be symmetric, that is,

$$A_{ij} = A_{ji}. \tag{39}$$

For $S^{\mathrm{pm}}$, the underlying matrix reads

$$A_{ij} = \frac{1}{\sum_{j\in\overline{N}_k} |\Omega_j|},$$

where $\overline{N}_k$ denotes the index set containing all child control volumes in the respective parent control volume $\overline{\Omega}_k$. The matrix obviously satisfies condition (39). Hence, the underlying matrix of $S^{\mathrm{pm}}$ is symmetric, and $S^{\mathrm{pm}}$ is proven to be a self-adjoint operator. Due to this, $S^{\mathrm{pm}}$ also fulfills the conservation condition (35). Proof of any self-adjointness of $S^{\mathrm{sm}}$, $S^{\mathrm{tf}}$, and $S^{\mathrm{sf}}$ and, thus, satisfaction of the conservation condition (35) may be done following the principles mentioned above.

Finally, the validity of (19) in a complete sense (i.e., explicit representation of all terms in (19)) with respect to the subgrid viscosity term remains to be analyzed. For the discrete smooth filters, large-scale boundaries (i.e., $\overline{\Gamma}_i$) and small-scale boundaries (i.e., $\Gamma'_i$) subject to (20) are not explicitly distinguished. Thus, it is trivial to verify that these filters, in contrast to the scale-separating operators based on combined multigrid operators, do not satisfy (19) in a complete sense. This is due to the fact that the third term in the second line of (19) cannot be represented. Nevertheless, there is also a crucial difference between $S^{\mathrm{pm}}$ and $S^{\mathrm{sm}}$ in this context: there is no large-scale (subgrid) viscous flux for $S^{\mathrm{pm}}$ across the small-scale boundary subject to (20). This may already be pointed out for the 1-D case by surveying Figs. 2(a) and (b). It is obvious that $S^{\mathrm{pm}}$ yields the same value in both child control volumes of any parent control volume, see Fig. 2(a). Thus, there is no derivative (or gradient in 2-D and 3-D, respectively) of the large-scale function at inner small-scale boundaries within any parent control volume, and the large-scale part of the subgrid viscosity term at these boundaries is ensured to be zero. As a result, (19) may be specified for $S^{\mathrm{pm}}$ as

$$B^{\mathrm{FV}}_{\mathrm{NS}}\left(\boldsymbol{v}^h_i, q^h_i; \boldsymbol{u}^h, p^h\right) - \left(\boldsymbol{v}'^h_i, \nu'_{\mathrm{T}}\left(\nabla \boldsymbol{u}^h\right)\cdot \boldsymbol{n}\right)_{\Gamma'_i} = \left(\boldsymbol{v}^h_i, \boldsymbol{f}\right)_{\Omega}. \tag{40}$$

Fig. 2(b) illustrates the configuration for $S^{\mathrm{sm}}$, where, in general, a non-zero large-scale subgrid viscosity term has to be expected even at the inner (small-scale) boundaries. Thus, (40) is not valid in this case. In Fig. 3, the definition of large- and small-scale boundaries in the finite volume method is re-emphasized

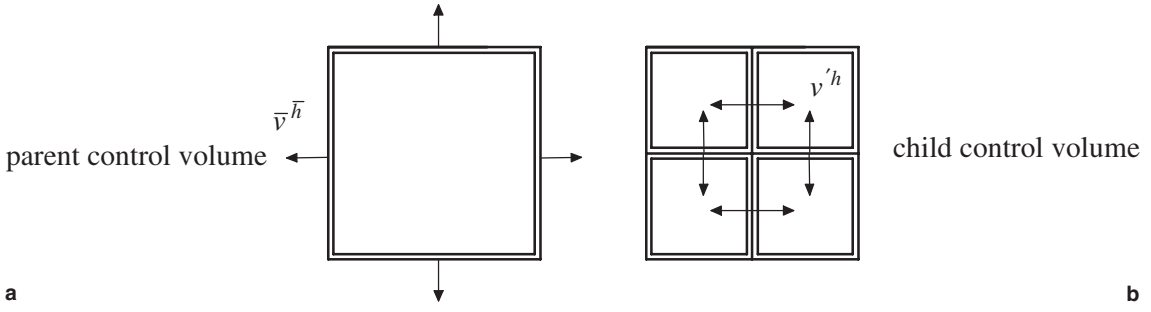


Fig. 3. Geometrical locations of weighting functions in the FVM for a 2-D case: (a) large-scale; (b) small-scale.

for the 2-D case. The large-scale weighting function $\overline{\boldsymbol{v}}^h$ is exclusively defined on the large-scale boundaries belonging to the parent control volume, as shown in Fig. 3(a). The small-scale weighting function $\boldsymbol{v}'^h$ has non-zero values only on the inner boundaries of the child control volumes, see Fig. 3(b).

### 3.3. Treatment of Dirichlet boundaries

Periodic boundaries used in the numerical examples at the end of the present study do not pose any problems for the scale-separating operators defined in the preceding sections. Hence, it may be focussed on the remaining Dirichlet boundaries. Dirichlet boundaries are implemented in CDP-α via so-called "fake" control volumes. The fake control volumes are actually located outside of the problem domain $\Omega$ and "mirror" their corresponding control volume inside of the problem domain $\Omega$ (i.e., they are assigned the same geometry as the corresponding inner control volume). In particular, the center of the fake control volume is located at double the distance from the center of the inner control volume to the Dirichlet boundary. Thus, the fake control volume center is located at the same distance from the Dirichlet boundary as the inner control volume center. In Fig. 4, the situation in a 1-D setting is depicted for simplicity. Nevertheless, it may easily be generalized to an unstructured 3-D case by locating the center of the fake control volume at double the distance from the center of the inner control volume normal to the respective face of the inner control volume on the Dirichlet boundary to the center of this face.

In Fig. 4, the scalar value $u_{\mathrm{f}}^h$ in the fake control volume $\Omega_{\mathrm{f}}$ is defined by the value $u_i^h$ in the neighbouring inner control volume $\Omega_{\mathrm{i}}$ as well as the (discrete) Dirichlet boundary condition $g^h$ subject to

$$u_{\mathrm{f}}^h = 2g^h - u_i^h. \tag{41}$$

For one of the scale-separating operators, $S^{\mathrm{sm}}$, it is necessary to define Dirichlet boundary conditions for the large-scale velocity analogous to (5) for the calculation of the large-scale velocity at the center of boundary control volumes. As an assumption for this purpose, the fulfillment of the Dirichlet boundary condition is entirely attributed to the large-scale velocity, such that

$$\overline{\boldsymbol{u}} = \boldsymbol{g} \quad \text{on } \Gamma \times (0,T), \tag{42}$$

which implies

$$\boldsymbol{u}' = \boldsymbol{0} \quad \text{on } \Gamma \times (0,T).$$

Thus, (41) is also valid for the large-scale values, such that

$$\overline{u}_{\mathrm{f}}^h = 2g^{\overline{h}} - \overline{u}_i^h.$$

**Remark.** Since $\boldsymbol{g} = \boldsymbol{0}$ at all channel walls in the simulations at the end of the present study, besides periodic boundary conditions at all other channel boundaries, the large-scale Dirichlet boundary condition (42) is exact and actually does not represent an assumption, which it, however, would amount to for non-zero $\boldsymbol{g}$. For more complex boundary conditions, more sophisticated assumptions for the distribution of the

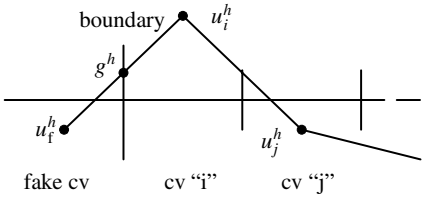


Fig. 4. Implementation of Dirichlet boundaries in a 1-D setting.

complete Dirichlet boundary condition (5) among large- and small-scale Dirichlet boundary conditions might become necessary.

The essential difference between the various scale-separating operators becomes obvious in the calculation of the large-scale value $\overline{u}_i^h$. Both discrete smooth filters of Section 3.1 have to take into account fake values in this particular implementation. For $S^{\mathrm{tf}}$, the large-scale value in $\Omega_i$ is obtained as

$$\overline{u}_i^h = \tfrac{1}{4}\left(u_{\mathrm{f}}^h + 2u_i^h + u_j^h\right),$$

where $u_j^h$ denotes the value in the control volume $\Omega_j$, as shown in Fig. 4. $S^{\mathrm{sf}}$ yields an analogous formula with different coefficients. In both cases, the definition of the large-scale Dirichlet boundary condition is required for the calculation of the large-scale flux terms through the faces at the Dirichlet boundary. As aforementioned, in case of $S^{\mathrm{sm}}$, $\overline{u}_i^h$ depends on the definition of the large-scale Dirichlet boundary condition (42). This is due to the fact that the parent grid gradient operator $\nabla^{\overline{h}}$ in the prolongation step (32) takes into account the respective large-scale fake value as defined in (33), which, in turn, is subject to (42). It may be contrasted to the discrete smooth filters, where the necessary fake values depend on the complete Dirichlet boundary condition (5). The only scale-separating operator entirely relying on values inside the problem domain $\Omega$ (excluding the domain boundary $\Gamma$) is $S^{\mathrm{pm}}$.

### 3.4. Characteristic length-scale ratios associated with the scale-separating operators

The determination of the characteristic length scale associated with the various scale-separating operators is an important ingredient of the dynamic modeling procedure to be presented in Section 4. More precisely, the ratio of the characteristic length scales $\overline{h}/h$ is the only parameter required for the dynamic models. The importance of the accuracy of this ratio was emphasized in [41,59]. Nevertheless, the actual value of the characteristic length scale of the basic discretization $h$ is required for the standard Smagorinsky model based on a constant coefficient. As usual, the characteristic length scale of the child control volume $\Omega_i$ is assumed to be the cube root of the respective measure, that is,

$$h_i = |\Omega_i|^{1/3}. \tag{43}$$

A straightforward extension of (43) leads to the characteristic length scale of the parent control volume $\overline{\Omega}_i$, which contains the child control volume $\Omega_i$, as

$$\overline{h}_i = |\overline{\Omega}_i|^{1/3}$$

and, thus, to a characteristic length-scale ratio

$$\frac{\overline{h}_i}{h_i} = 2 \tag{44}$$

in the case of an isotropic refinement of each parent control volume by a factor of 2, as described in Section 3.2.

The characteristic length-scale ratio (44) may be assigned, for the time being, to the restriction operator $R$, which is identical for both scale-separating operators $S^{\mathrm{pm}}$ and $S^{\mathrm{sm}}$, as it was also done in [64]. In that study, the ratio 2 was assigned to a "filter" operator similar to $S^{\mathrm{pm}}$, given that another filter operator corresponding to $S^{\mathrm{sm}}$ was not considered. In the present study, however, two obviously different prolongation operators have been introduced, a constant prolongation $P^{\mathrm{p}}$ and a linear prolongation $P^{\mathrm{s}}$. The first question is now, which one of the two scale-separating operators $S^{\mathrm{pm}}$ and $S^{\mathrm{sm}}$ indeed has to be assigned to the ratio 2. In this author's view, as a first conclusion, the ratio 2 should only be attributed to $S^{\mathrm{sm}}$, since this scale-separating operator assumes a linear interpolation of the solution function on the child grid as well as on the parent grid based on the values at the control volume centers, see Fig. 2(b) for a one-dimensional

representation. Considering the solid line in the upper part of Fig. 2(b) and the dashed line in the middle part of Fig. 2(b), it is stated that both the interpolation of the values on the child grid and the interpolation of the large-scale values on the parent grid are *piecewise linear* interpolation curves. Thus, both curves exhibit the same character and they are only distinguished by the fact that one of the curves is assigned to a grid which is coarser by a factor of 2. By comparing Fig. 2(a) to (b), the essential difference of the two operators in this context becomes obvious. Whereas the curve in the upper part of Fig. 2(a) represents a piecewise linear interpolation of the values on the child grid, the curve in the middle part of Fig. 2(a) consists of, on the one hand, *piecewise constant* interpolations inside of each parent control volume and, on the other hand, *piecewise linear* interpolations which cannot be assigned to the characteristic length scale $\overline{h}$ (i.e., the one twice as large as $h$ in the present case). Thus, a second question arises, asking whether the characteristic length-scale ratio for $S^{\mathrm{pm}}$ is larger or smaller than the one for $S^{\mathrm{sm}}$. Given the theoretical considerations so far, a final assessment related to this second question does not appear to be clear at this stage. However, the present study aims at estimating the characteristic length-scale ratio depending on the actual results of the numerical simulations.

## 4. Subgrid-scale modeling within the multiscale environment

### 4.1. Smagorinsky model

The Smagorinsky model [57] was the first subgrid-scale model historically and is still a commonly used one due to its attractive simplicity. Adopting the usual filter-related notation to the underlying situation where the resolved part of the velocity is defined by the discretization with characteristic length scale $h$, the subgrid viscosity can be expressed as

$$v_{\mathrm{T}} = (C_{\mathrm{S}}h)^2|\boldsymbol{\varepsilon}(\boldsymbol{u}^h)|. \tag{45}$$

The Smagorinsky model constant is denoted by $C_{\mathrm{S}}$ in (45). The actual evaluation of (45) is performed in every child control volume $\Omega_i$ using the length-scale definition (43) for the calculation of $h_i$, so that a value $v_{\mathrm{T},i}$ in every child control volume is obtained. The weak point of the Smagorinsky model is represented by the constant $C_{\mathrm{S}}$ in (45). Numerous authors have addressed this issue, and perhaps the most important improvement has been achieved by the dynamic modeling procedure in [12], which will be dealt with in the following section. Despite the well-known flaws of the constant-coefficient Smagorinsky model, the integration of this simple model in the framework of the variational multiscale method has already led to good results for a number of test cases. The present study focuses on the specific modification of the model restricting the dependence on the small scales subject to

$$v'_{\mathrm{T}} = (C_{\mathrm{S}}h)^2|\boldsymbol{\varepsilon}(\mathbf{u}'^h)| = (C_{\mathrm{S}}h)^2|\boldsymbol{\varepsilon}(\boldsymbol{u}^h - \overline{\boldsymbol{u}}^h)|, \tag{46}$$

which was named ''small–small'' model in [26] and seems to be the most natural version within the multiscale formalism. Other versions are a ''large–small'' model using only the large-scale part of the velocity for the calculation of the rate-of-deformation tensor $\boldsymbol{\varepsilon}$, which was mainly introduced for achieving some gain in computational efficiency in [26], and the original definition in (45) as an ''all–small'' model, which was applied, for instance, in a dynamic modeling procedure in [23]. As for (45), the actual evaluation of (46) is performed in every child control volume $\Omega_i$, using the same length scale definition (43) for the calculation of $h_i$. In the end, a value $v'_{\mathrm{T},i}$ in every child control volume is obtained. Test simulations in the course of this work have shown at most comparable results for the large–small and all–small model with respect to the small–small model, but no superior results. Thus, applications of the Smagorinsky model based on a constant coefficient are executed and reported using (46) exclusively. The constant $C_{\mathrm{S}}$ is chosen to be 0.1 for the channel flow simulations according to the original choice in [8].

### 4.2. Dynamic modeling procedure based on the classical Germano identity

The dynamic modeling procedure proposed in [12] enables a computation of the constant $C_S$ as a function of time and position. Thus, the model *constant* $C_S$ will now be considered a model *parameter* in the context of the dynamic modeling procedure. The procedure is basically not restricted to using the Smagorinsky model as the underlying model, although it has usually been applied with this model. It is interesting to note that the dynamic modeling procedure already distinguishes large resolved scales, small resolved scales, and unresolved scales explicitly. This mirrors the type of scale separation in the variational three-scale formulation.

The dynamic modeling procedure is based on the Germano identity (see, e.g., [11]), which will be named the "classical Germano identity". With this labeling, it is explicitly distinguished from the "variational Germano identity", which has recently been introduced in [51]. Due to the pointwise formulation of the classical Germano identity, the dynamic procedure starts with a pointwise formulation of the Navier–Stokes equations for the discretized variables $\boldsymbol{u}^h$ and $p^h$. The momentum equation is given as

$$\frac{\partial \boldsymbol{u}^h}{\partial t} + \nabla \cdot (\boldsymbol{u}^h \otimes \boldsymbol{u}^h) + \nabla p^h - 2\nu \nabla \cdot \boldsymbol{\varepsilon}\left(\boldsymbol{u}^h\right) + \nabla \cdot \boldsymbol{\tau}^h = \boldsymbol{f}^h, \tag{47}$$

where the subgrid-scale stress tensor is defined as

$$\boldsymbol{\tau}^h = (\boldsymbol{u} \otimes \boldsymbol{u})^h - \boldsymbol{u}^h \otimes \boldsymbol{u}^h. \tag{48}$$

Note that in (47) and (48) the usual filtered formulation is replaced by the actual implicit scale-separation based on the chosen discretization with characteristic length scale $h$. The "test filter" is replaced by the scale-separating operators of Section 3. Thus, the analog of the "subtest"-scale stress tensor can be expressed as

$$\overline{\boldsymbol{\tau}}^h = \overline{(\boldsymbol{u} \otimes \boldsymbol{u})^h} - \overline{\boldsymbol{u}}^h \otimes \overline{\boldsymbol{u}}^h = S\left[(\boldsymbol{u} \otimes \boldsymbol{u})^h\right] - S[\boldsymbol{u}^h] \otimes S[\boldsymbol{u}^h]. \tag{49}$$

The basic procedure yields a value for the parameter $C_S$ at every degrees of freedom of the child grid. The classical Germano identity related to the child grid discretization level states the following:

$$\boldsymbol{L}^h = \overline{\boldsymbol{\tau}}^h - S[\boldsymbol{\tau}^h], \tag{50}$$

where $\boldsymbol{L}^h$ can be obtained as

$$\boldsymbol{L}^h = \overline{\boldsymbol{u}^h \otimes \boldsymbol{u}^h} - \overline{\boldsymbol{u}}^h \otimes \overline{\boldsymbol{u}}^h = S[\boldsymbol{u}^h \otimes \boldsymbol{u}^h] - S[\boldsymbol{u}^h] \otimes S[\boldsymbol{u}^h]$$

by inserting (48) and (49) into (50). The Smagorinsky model is now assumed as an appropriate modeling term at both discretization levels. Furthermore, it should account for the fact that the Smagorinsky model within the subgrid viscosity concept is basically a "trace-free" model for incompressible flow (i.e., the rate-of-deformation tensor $\boldsymbol{\varepsilon}$, which will appear in the following model formulation, has a zero trace). Thus, only the deviatoric part, $\operatorname{dev}\boldsymbol{L}^h$, of the tensor $\boldsymbol{L}^h$ in (50) can be modeled as

$$\operatorname{dev}\boldsymbol{L}^h = \boldsymbol{L}^h - \tfrac{1}{3}\operatorname{tr}\boldsymbol{L}^h \boldsymbol{I} \approx -2(C_S\overline{h})^2 |S[\boldsymbol{\varepsilon}(\boldsymbol{u}^h)]| S[\boldsymbol{\varepsilon}(\boldsymbol{u}^h)] + S[2(C_S h)^2 |\boldsymbol{\varepsilon}(\boldsymbol{u}^h)| \boldsymbol{\varepsilon}(\boldsymbol{u}^h)], \tag{51}$$

where $\boldsymbol{I}$ denotes the identity tensor. Both the rate-of-deformation tensor of the finite-dimensional velocity field $\boldsymbol{\varepsilon}(\boldsymbol{u}^h)$ and its scale-separated value $S[\boldsymbol{\varepsilon}(\boldsymbol{u}^h)]$ will be ensured to have a trace as close to zero as possible in the actual numerical simulations, see Section 5 for elaboration. It is assumed that $C_S$ is at least constant over one control volume of the parent grid or the appropriate measure for the discrete smooth filters, respectively. Hence, (51) may be rewritten as

$$\operatorname{dev}\boldsymbol{L}^h \approx (C_S h)^2 \left( 2S\left[|\boldsymbol{\varepsilon}(\boldsymbol{u}^h)| \boldsymbol{\varepsilon}(\boldsymbol{u}^h)\right] - 2\left(\frac{\overline{h}}{h}\right)^2 |S[\boldsymbol{\varepsilon}(\boldsymbol{u}^h)]| S[\boldsymbol{\varepsilon}(\boldsymbol{u}^h)] \right) = (C_S h)^2 \boldsymbol{M}^h. \tag{52}$$

The calculation of the parameter expression $(C_S h)^2$ on the right-hand side of (52) aims to minimize the error tensor

$$\boldsymbol{E}^h = \operatorname{dev} \boldsymbol{L}^h - (C_S h)^2 \boldsymbol{M}^h. \tag{53}$$

Using the least-squares approach proposed in [40], the formula for the parameter expression reads

$$(C_S h)^2 = \frac{\operatorname{dev} \boldsymbol{L}^h \boldsymbol{M}^h}{\boldsymbol{M}^h \boldsymbol{M}^h}. \tag{54}$$

Potential numerical problems may have to be faced related to either unbounded or negative (and, thus, anti-dissipative) values for the parameter expression $(C_S h)^2$, jeopardizing the stability of the simulation. As an artificial measure to account for this, both numerator and denominator in (54) are averaged over the homogeneous planes of the channel in the numerical simulations at the end of the present study. Additionally, clipping is performed (i.e., potential negative values for the parameter expression $(C_S h)^2$ are set to zero artificially).

**Remark.** The application of the scale-separating operators based on combined multigrid operators opens up the opportunity to determine the values for the parameter $C_S$ only at the degrees of freedom of the parent grid subject to

$$\overline{\boldsymbol{\tau}}^{\bar{h}} = \left(\overline{\boldsymbol{u} \otimes \boldsymbol{u}}\right)^{\bar{h}} - \overline{\boldsymbol{u}}^{\bar{h}} \otimes \overline{\boldsymbol{u}}^{\bar{h}} = R\left[(\boldsymbol{u} \otimes \boldsymbol{u})^h\right] - R[\boldsymbol{u}^h] \otimes R[\boldsymbol{u}^h] \tag{55}$$

by using the restriction operator exclusively. In order to maintain comparability with the other scale-separating operators, (49) will be preferred to (55) in the numerical simulations in Section 6. Nevertheless, the alternative procedure will also be briefly outlined in the following.

The classical Germano identity related to the parent grid discretization level reads

$$\boldsymbol{L}^{\bar{h}} = \overline{\boldsymbol{\tau}}^{\bar{h}} - R[\boldsymbol{\tau}^h], \tag{56}$$

where $\boldsymbol{L}^{\bar{h}}$ can be obtained as

$$\boldsymbol{L}^{\bar{h}} = \overline{\boldsymbol{u}^h \otimes \boldsymbol{u}^h}^{\bar{h}} - \overline{\boldsymbol{u}}^{\bar{h}} \otimes \overline{\boldsymbol{u}}^{\bar{h}} = \boldsymbol{R}[\boldsymbol{u}^h \otimes \boldsymbol{u}^h] - \boldsymbol{R}[\boldsymbol{u}^h] \otimes \boldsymbol{R}[\boldsymbol{u}^h]$$

by inserting (48) and (55) into (56). Replacing the scale-separating operator $S$ by the restriction operator $R$ as well as the superscript $h$ by the superscript $\bar{h}$ in (51)–(54) then yields the respective equations for the alternative case.

## 5. Aspects of the implementation

All numerical simulations which will be presented in the upcoming section have been done using the CDP-α code. CDP is an unstructured finite-volume-based CFD code designed for LES of variable density low Mach-number flows on very large grids, using massively parallel computers. It was developed at Stanford University as part of the Department of Energy's Accelerated Strategic Computing Initiative (ASCI). In particular, it was intended to be used for LES of reacting multiphase flow in complex geometry. It is written in Fortran 90 and uses MPI for parallelization. CDP-α is the new redesigned and rewritten version of CDP (see [52]), initiated in 2003. The reader may consult a series of Annual Research Briefs of the Center for Turbulence Research, the latest two being [42,18], for a detailed description of the several development stages leading to the current code. A basic version of CDP-α suited for the numerical simulation of incompressible flows has served as a foundation for implementing the developments of the present work.

The temporal and spatial discretization underlying CDP-α is described in [15]. The main features are the use of a fractional-step procedure with a four-step scheme (see, e.g., [3]) and the momentum interpolation

method for unstructured colocated grids according to [35]. The Crank–Nicolson scheme, a fully implicit time-stepping scheme of second-order accuracy, is applied to the convective and viscous terms. The nonlinear convective term is linearized about the result of the previous time step. All spatial and temporal approximations are of second-order accuracy, as shown in [15]. Furthermore, discrete conservation of energy is enforced. The discrete representation of the convective and the pressure term are the crucial aspects for guaranteeing discrete conservation of energy. These issues are addressed in detail in [43]. The particular reconstruction for the pressure term used in the current version of CDP-$\alpha$ is described in [19]. Plots quantifying the discrete conservation of energy for a number of test problems may be found in [43,19]. The momentum equation in the first step of the fractional-step procedure is solved using a simple iterative SOR solution procedure. For the solution of the pressure Poisson equation in the third step of the fractional-step procedure, an algebraic multigrid solver is used. See [18] for the details as well as some investigations concerning the performance of this multigrid solver.

The divergence of the velocity is monitored throughout the simulation. It is checked several times during each time step by calculating the divergence of the velocity in each control volume and writing out the maximum and minimum values for all control volumes. The divergence of the velocity has been calculated to be less than $10^{-12}$ in all control volumes for all numerical simulations conducted for the present study. In this connection, the trace of the rate-of-deformation tensor of the finite-dimensional velocity field $\boldsymbol{\varepsilon}(\boldsymbol{u}^h)$, which is equivalent to the discrete divergence of the velocity, and the trace of its scale-separated value $S[\boldsymbol{\varepsilon}(\boldsymbol{u}^h)]$ have also been ensured to be less than $10^{-12}$ in all control volumes. The monitoring of the trace of the scale-separated rate-of-deformation tensor is obviously only necessary for simulations with a dynamic modeling procedure. For the (relatively simple) grid generation in the case of the channel simulations, a preprocessing program called CART2CDP is applied, enabling the generation of grids within simple cartesian geometries. Afterwards, the preprocessing produces $N_\mathrm{p}$ separate grid partition files, where $N_\mathrm{p}$ denotes the number of processors used for the simulation with CDP-$\alpha$. For a detailed description of the preprocessing stage, it is again referred to [18].

For the simulations in this work, the (coarser) parent grid is initially generated during a first preprocessing stage, performed as a single-processor procedure. Afterwards, the (finer) child grid is obtained by an isotropic hierarchical subdivision during a second preprocessing stage. The first preprocessing stage and, thus, the initial parent grid generation is executed in a sequential program independent of CDP-$\alpha$, as mentioned above. However, the second preprocessing may be done in parallel as part of CDP-$\alpha$. For grids containing a very high number of control volumes, substantial savings in computing time may be achieved by this strategy in comparison to a generation of the child grid during the first single-processor preprocessing stage. The generation of a child grid starting from a (coarser) parent grid is used for all simulations in Section 6 (i.e., also for the calculations using discrete smooth filters as well as the non-multiscale calculations), in order to ensure comparability in terms of the grid geometry.

As already mentioned in Section 3.2, a complete parent–child knowledge base is set up (i.e., every parent knows about every child and vice versa). The arrays covering the geometrical information for the child grid are created on the basis of the existing geometrical information for the parent grid. The respective parent control volume is transformed to a unit control volume and predetermined standardized data for the respective unit geometry is retrieved. Afterwards, it is transformed back to the actual control volume, including all new child control volumes. Aside from the required geometrical information, the complete set of connectivity arrays for the child-control-volume-to-child-face relation, which is necessary for the finite volume code, is developed from the existing connectivity arrays for the parent grid. In particular, (outer) faces assigned to the large-scale boundary $\overline{\Gamma}_i$ are explicitly distinguished from (inner) faces belonging to the small-scale boundary $\Gamma'_i$, a distinction unnecessary in usual finite volume codes. For the trapezoidal filter (24)–(25), a connectivity array covering the relation between child control volumes and child nodes has to be provided. An additional array for the connectivity of child control volumes and child edges, besides the already existing connectivity arrays, is required for Simpson's filter (26)–(27). As a final step of the second (parallel) preprocessing stage, the processor communication pattern for the child grid is generated.

The four scale-separating operators introduced in Section 3 are covered by separate subroutines, which are called at several stages of the calculation procedure. At the beginning of each time step, an initial scale separation is performed for the velocity field, in order to provide values for the calculation of coefficients for the matrix and right-hand side related to the momentum equation. Within the actual solution procedure, the respective scale-separating subroutine is executed at the beginning of each solver iteration step, in order to determine the updated large-scale velocity field for the residual calculation. All of these calls are not required for $S^{\mathrm{pm}}$ due to the validity of (40) in this case. *This is a source of substantial savings in computational effort in comparison to the other operators*. Additional calls of the scale-separating subroutines or, for $S^{\mathrm{pm}}$, the only calls, respectively, are necessary during a dynamic modeling procedure.

## 6. Numerical example: turbulent channel flow

### 6.1. Setup for numerical simulations

Five important aspects related to the setup for the numerical simulations are addressed in this section: the channel dimensions, the initial condition, the boundary conditions (including the driving mechanism), the spatial and the temporal resolution. A sketch of the channel geometry is displayed in Fig. 5.

Flows at two different Reynolds numbers, $Re_\tau = u_\tau\ \delta_c/\nu = 180$ and $Re_\tau = 590$, are performed, marking the lower and upper end of the study in [48]. The turbulent wall-shear velocity $u_\tau = \sqrt{\tau_w}$, where $\tau_w$ denotes the wall-shear stress, and the channel half-width $\delta_c$ (see Fig. 5) define the Reynolds number $Re_\tau$, besides the kinematic viscosity $\nu$. According to [48], the *channel dimensions* are chosen to be slightly different for the two cases. For the low Reynolds number case, $L_1 \times L_2 \times L_3 = 2\pi\delta_c \times 2\delta_c \times (4/3)\pi\delta_c$ and, for the high Reynolds number case, $L_1 \times L_2 \times L_3 = 2\pi\delta_c \times 2\delta_c \times \pi\delta_c$, where the channel half-width $\delta_c$ is fixed to be of unit length.

A parabolic velocity profile perturbed by a random velocity fluctuation of 10%-amplitude of the bulk mean streamwise velocity represents the *initial condition* $\boldsymbol{u}_0$ for the velocity field:

$$
\begin{aligned}
u_1(x_2, t=0) &= u_{1,c}(1 - x_2^2) + 0.1 u_{1,m}\psi_{\mathrm{ran}},\\
u_2(x_2, t=0) &= 0.1 u_{1,m}\psi_{\mathrm{ran}},\\
u_3(x_2, t=0) &= 0.1 u_{1,m}\psi_{\mathrm{ran}},
\end{aligned}
$$

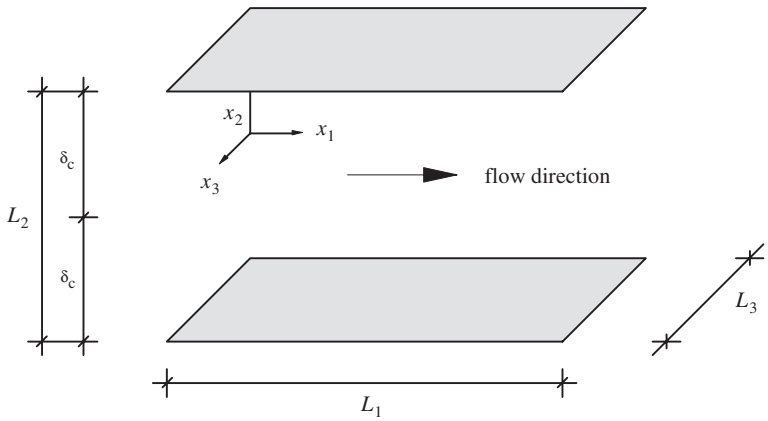


Fig. 5. Sketch of channel geometry.

where $u_{1,c}$ denotes the streamwise velocity at the centerline of the channel, $u_{1,m}$ the bulk mean streamwise velocity, and $\psi_{ran}$ a random number, taken to be in the interval $[-1, 1]$. In order to obtain the initial velocity field at the beginning of each simulation, a value for $\psi_{ran}$ is randomly generated at the center of each control volume using the Fortran intrinsic function "ran". For the lower Reynolds number case, it is chosen that $u_{1,c} = 25$ and, hence, $u_{1,m} = 2u_{1,c}/3 = 16.7$ for the underlying parabolic profile. The values for the higher Reynolds number case are $u_{1,c} = 28$ and, accordingly, $u_{1,m} = 18.7$.

No-slip *boundary conditions* are applied at the upper and lower wall perpendicular to the $x_2$-direction, see Fig. 5. In $x_1$- as well as $x_3$-direction, periodic conditions for the velocity are applied on the boundaries. Additionally, a *driving mechanism* for the flow has to be provided. This is done by imposing a body force in form of a driving pressure gradient in the streamwise $x_1$-direction. Thus, the body force vector reads

$$f = \begin{bmatrix} f_p \\ 0 \\ 0 \end{bmatrix} = \begin{bmatrix} 1.0 \\ 0 \\ 0 \end{bmatrix}.$$

The specific choice of a unit value for $f_p$ aims at a unit value for the turbulent wall-shear velocity $u_\tau$ in the statistically steady state, subject to the relation

$$u_\tau = \sqrt{f_p \delta_c} - \sqrt{f_p} = 1.0$$

(see, e.g., [9]).

Relatively coarse *spatial resolutions* using 32 control volumes in all coordinate directions for the lower Reynolds number case and 64 control volumes in all coordinate directions for the higher Reynolds number case, respectively, are employed. The distribution of control volumes in the wall-normal $x_2$-direction obeys a cosine function, refining towards the walls for the parent grid, with the subsequent isotropic subdivision procedure applied. As usual, the characteristic length scales are expressed in non-dimensional length units $h^+ = h/\delta_v = hu_\tau/\nu$, scaling the actual characteristic control volume length by the viscous length scale $\delta_v$. The control volume lengths in the respective coordinate directions correspond to $h_1^+ = 35.34$, $h_{2,\min}^+ = 1.73$, $h_{2,\max}^+ = 17.56$, and $h_3^+ = 23.56$ for the lower Reynolds number case and $h_1^+ = 57.92$, $h_{2,\min}^+ = 1.42$, $h_{2,\max}^+ = 28.92$, and $h_3^+ = 28.96$ for the higher Reynolds number case, respectively. Results for finer resolutions in both cases (i.e, doubling the number of control volumes in the wall-normal and spanwise direction) may be found in an extended version of the present study [15].

The respective time-step value for the *temporal resolution* is evaluated based on a fixed choice of the CFL number. The CFL number is calculated according to the definition in [35]. For both Reynolds numbers, the CFL number is prescribed to be 0.65. 5000 time steps are performed to allow the flow to develop, and the statistics are collected during another 5000 time steps. The flow is assumed to be statistically stationary during the statistical period. The average value of the actual time steps during the statistical period, expressed in wall units $\delta t^+ = \delta t u_\tau^2/\nu$, ranges from 0.71 up to 0.73 (0.86) for the lower Reynolds number case and from 0.83 up to 0.92 (1.00) for the higher Reynolds number case. The notably higher values in parentheses are obtained for calculations which simply apply the Smagorinsky model in a non-multiscale environment. The average value of the actual time step corresponds to an overall averaging period, expressed in wall units $T_{av}^+ = T_{av} u_\tau^2/\nu$, ranging from 3550 up to 3650 (4300) and from 4150 up to 4600 (5000), respectively. All of the actual time-step values are expected to be considerably less than the Kolmogorov time scale and, hence, to fulfill the condition formulated in [3].

### 6.2. Compared values and methods

Decomposing, for instance, the streamwise component $u_1$ of the velocity into a mean value $\langle u_1 \rangle$ and a fluctuating part $\tilde{u}_1$ in the statistical sense yields for the underlying case an extended equation as

$$u_1 = \langle u_1 \rangle + \tilde{u}_1 = \langle \overline{u}_1^h + u_1'^h + \hat{u}_1 \rangle + \tilde{u}_1 = \langle u_1^h \rangle + \langle \hat{u}_1 \rangle + \tilde{u}_1.$$

As usual in LES, it is assumed that $\langle \hat{u}_1 \rangle \approx 0$ (i.e., the unresolved scales do not contribute to the average value). In the following sections, the mean streamwise resolved small-scale velocity $\langle u_1'^h \rangle$ is investigated explicitly, besides the usual comparison of the mean streamwise resolved velocity $\langle u_1^h \rangle$. Mean values are obtained by averaging over all time steps of the statistical period as well as over homogeneous $x_1$–$x_3$ planes. Both mean values are scaled by the wall-shear velocity $u_\tau$ in the respective diagrams.

The components of the Reynolds stress tensor $\boldsymbol{\tau}^{\mathrm{R}}$ are expanded in a similar way. The expansion, for instance, for the component $\tau_{11}^{\mathrm{R}}$ reads

$$\begin{aligned}
\tau_{11}^{\mathrm{R}} &= \langle \tilde{u}_1 \tilde{u}_1 \rangle = \langle u_1 u_1 \rangle = \langle u_1 \rangle \langle u_1 \rangle \\
&= \left\langle \left( \overline{u}_1^h + u_1'^h + \hat{u}_1 \right) \left( \overline{u}_1^h + u_1'^h + \hat{u}_1 \right) \right\rangle - \langle \overline{u}_1^h + u_1'^h + \hat{u}_1 \rangle \langle \overline{u}_1^h + u_1'^h + \hat{u}_1 \rangle \\
&\approx \boldsymbol{\tau}_{11}^{\mathrm{R},h} = \langle u_1^h u_1^h \rangle - \langle u_1^h \rangle \langle u_1^h \rangle = \left\langle \left( \overline{u}_1^h + u_1'^h \right) \left( \overline{u}_1^h + u_1'^h \right) \right\rangle - \langle \overline{u}_1^h + u_1'^h \rangle \langle \overline{u}_1^h + u_1'^h \rangle \\
&\qquad = \left[ \langle \overline{u}_1^h \overline{u}_1^h \rangle - \langle \overline{u}_1^h \rangle \langle \overline{u}_1^h \rangle \right] + 2 \left[ \langle \overline{u}_1^h u_1'^h \rangle - \langle \overline{u}_1^h \rangle \langle u_1'^h \rangle \right] + \left[ \langle u_1'^h u_1'^h \rangle - \langle u_1'^h \rangle \langle u_1'^h \rangle \right],
\end{aligned} \tag{57}$$

where the approximation in the third line of (57) describes the common practice in LES, mentioned in [67]. The three terms in square brackets in the fourth line of (57) may be denoted as the large–large, large–small, and small–small contribution to the Reynolds stress tensor of the resolved scales in the third line. The values to be compared in the subsequent sections are the turbulent kinetic energy of the resolved scales

$$k^h = \tfrac{1}{2} \left( \langle u_1^h u_1^h + u_2^h u_2^h + u_3^h u_3^h \rangle - \langle u_1^h \rangle \langle u_1^h \rangle - \langle u_2^h \rangle \langle u_2^h \rangle - \langle u_3^h \rangle \langle u_3^h \rangle \right), \tag{58}$$

approximating half the trace of the Reynolds stress tensor $\boldsymbol{\tau}^{\mathrm{R}}$ and the small–small contribution to (58) subject to

$$k'^h = \tfrac{1}{2} \left( \langle u_1'^h u_1'^h + u_2'^h u_2'^h + u_3'^h u_3'^h \rangle - \langle u_1'^h \rangle \langle u_1'^h \rangle - \langle u_2'^h \rangle \langle u_2'^h \rangle - \langle u_3'^h \rangle \langle u_3'^h \rangle \right),$$

as a measure for the amount of scales attributed to the small-scale range by the various scale-separating operators. Both kinetic energy values are scaled by $u_\tau^2$ in the respective diagrams. All velocity and kinetic energy values are depicted as profiles in the wall-normal $x_2$-direction against the non-dimensional wall coordinate $x_2^+$. As usual, only half of the channel width is illustrated (i.e., the upper half-width here, ranging from $x_2 = 0$ to $x_2 = 1$, see Fig. 5). Defining $x_2^+ = (1 - x_2) u_\tau / \nu = (1 - x_2) Re_\tau / \delta_{\mathrm{c}}$, the upper wall is located at $x_2^+ = 0$ and the channel center at $x_2^+ = Re_\tau / \delta_{\mathrm{c}}$. Furthermore, the scaled profiles for $\langle u_1^h \rangle$ are quantified by evaluating the integral of their deviation from the respective DNS profiles in the $L_2$-norm $e_0^{\mathrm{u}}$ (i.e., an error measure with respect to the DNS results) in the wall-normal $x_2$-direction for the upper half-width of the channel subject to

$$e_0^{\mathrm{u}} = \frac{\left\| \langle u_1^h \rangle_{\mathrm{DNS}}^+ - \langle u_1^h \rangle_{\mathrm{LES}}^+ \right\|_0}{\| \langle u_1^h \rangle_{\mathrm{DNS}}^+ \|_0} = \left[ \frac{\int_{x_2=0}^{x_2=1} \left( \langle u_1^h \rangle_{\mathrm{DNS}}^+ - \langle u_1^h \rangle_{\mathrm{LES}}^+ \right)^2 \mathrm{d}x_2}{\int_{x_2=0}^{x_2=1} \left( \langle u_1^h \rangle_{\mathrm{DNS}}^+ \right)^2 \mathrm{d}x_2} \right]^{1/2}, \tag{59}$$

which is calculated as a discrete integral. The $x_2$-integral of the deviation for the turbulent kinetic energy $e_0^{\mathrm{k}}$ is evaluated analogously.

The discrete integral of the kinetic energy over the complete 3-D domain defined as

$$E^h = \frac{1}{2} \sum_{i=1}^{n_{\mathrm{cv}}} |\Omega_i| \boldsymbol{u}_i^h \boldsymbol{u}_i^h$$

is also determined for the complete velocity as well as for the large- and small-scale part of the velocity, respectively. Based on the discrete integral of the kinetic energy, a characteristic velocity $u_{\mathrm{char}}$, subject to

$$u_{\mathrm{char}} = \sqrt{2 \frac{E^h}{|\Omega|}}, \tag{60}$$

is defined. Replacing the complete discrete integral of the kinetic energy by the large- and small-scale part in (60) yields the characteristic large- and small-scale velocities $\overline{u}_{\mathrm{char}}$ and $u'_{\mathrm{char}}$, respectively. $u'_{\mathrm{char}}$ will be exploited as a rough measure to evaluate the actual characteristic length-scale ratio for the various scale-separating operators in relation to $S^{\mathrm{sm}}$ a posteriori. It is emphasized that this measure has to be handled with care. On the one hand, it might be dependent on the respective flow problem. However, since there is only one particular flow problem to be investigated in the present study, explicit conclusions may be drawn only within the scope of this particular problem. On the other hand, the character of the respective scale-separating operator has to be taken into account for any conclusions. For orthogonal projective operators (i.e., self-adjoint projectors), such as $S^{\mathrm{pm}}$, the total kinetic energy is explicitly split into a large-scale part and a small-scale part. For operators not fulfilling this prerequisite, ''cross'' parts have to be expected (i.e., the large- and the small-scale part are not explicitly separated).

Three different methods are compared:

- The dynamic Smagorinsky (DS) model based on the classical Germano identity in a non-multiscale application, with the subgrid viscosity subject to (45).
- The constant-coefficient Smagorinsky (CMS) model within the multiscale environment subject to (19) or (40), respectively, with the subgrid viscosity according to (46).
- The dynamic Smagorinsky (DMS) model based on the classical Germano identity within the multiscale environment subject to (19) or (40), respectively, with the subgrid viscosity according to (46).

All of these methods are investigated for the four different scale-separating operators $S^{\mathrm{pm}}$, $S^{\mathrm{sm}}$, $S^{\mathrm{tf}}$, and $S^{\mathrm{sf}}$, leading to 12 different methodical combinations overall. In the following diagrams, the acronym DMS-PM, for instance, indicates the variational multiscale LES incorporating a dynamic Smagorinsky model with the scale-separating operator $S^{\mathrm{pm}}$ applied. Results are also reported for simulations using the constant-coefficient Smagorinsky model in a non-multiscale environment (CS) as well as applying no model at all (NM), which represents a coarse (i.e., not sufficiently resolved) DNS. It should be emphasized that CMS is merely the combination of these last two approaches by applying no model to the large resolved scales and the constant-coefficient Smagorinsky model to the small resolved scales. All of the acronyms indicating the respective methods and scale-separating operators used in the numerical simulations are summarized in Tables 1 and 2, respectively. The computational effort required for the various methodical combinations will also be evaluated in the upcoming sections.

Table 1
Acronyms for methods used in the numerical simulations

| Acronym | Description |
|---|---|
| DNS | DNS (simulation results from [48]) |
| NM | LES with no subgrid-scale model at all (coarse DNS) |
| CS | Traditional LES with constant-coefficient-based Smagorinsky model |
| DS | Traditional LES with dynamic Smagorinsky model |
| CMS | Variational multiscale LES with constant-coefficient-based Smagorinsky model |
| DMS | Variational multiscale LES with dynamic Smagorinsky model |

Table 2
Acronyms for scale-separating operators used in the numerical simulations

| Acronym | Description |
|---|---|
| PM | Projective multigrid operator |
| SM | Smoothed multigrid operator |
| TF | Discrete smooth filter (trapezoidal rule) |
| SF | Discrete smooth filter (Simpson's rule) |

The characteristic length-scale ratio, which is required for the methods using the dynamic Smagorinsky model (i.e., DS and DMS), has to be selected a priori for the various scale-separating operators. For $S^{\mathrm{sm}}$, a characteristic length-scale ratio of 2 is chosen, as already discussed in Section 3.4. Based on preliminary results from CMS simulations, the characteristic length-scale ratio for all DS and DMS simulations is set to 2.5 for $S^{\mathrm{pm}}$.

**Remark.** For $S^{\mathrm{tf}}$ and $S^{\mathrm{sf}}$, various characteristic length-scale ratios may be found and were actually used in the literature. In [41], the ratio was, on the one hand, determined based on the second moment of the filter function according to [39], which produced values of $\sqrt{6}$ and 2 for $S^{\mathrm{tf}}$ and $S^{\mathrm{sf}}$, respectively. Similar values were achieved by an optimized approximation in [55]. On the other hand, the filter transfer function was offered as a more general alternative for the determination of the characteristic filter width for filters with vanishing moments in [41]. Based on the criterion that the filter width is taken to be proportional to the inverse wave number where the filter transfer function falls to 0.5, values of 2 and 1.5 for $S^{\mathrm{tf}}$ and $S^{\mathrm{sf}}$ were obtained. This criterion was also used in [59]. All of these investigations were actually performed in a 1-D setting, but may be extended to the 3-D case in a similar way as the actual filter is extended. Two simpler definitions for the ratio were introduced for kernel filters in the sense of (1) in [64]. The first one is based on the $L_2$-norm of the kernel. Transferring this definition to the discrete 1-D case yields values of 2.67 and 2 for $S^{\mathrm{tf}}$ and $S^{\mathrm{sf}}$, respectively. The second one is based on the central value of the filter function, and its transfer to the discrete 1-D case reveals ratios of 2 and 1.5 for $S^{\mathrm{tf}}$ and $S^{\mathrm{sf}}$, respectively. Recapitulating, it is stated that ambiguous specifications regarding the choice of the characteristic length-scale ratio for $S^{\mathrm{tf}}$ and $S^{\mathrm{sf}}$ may be found in the respective literature (i.e., 2.67, $\sqrt{6}$, and 2 for $S^{\mathrm{tf}}$ as well as 2 and 1.5 for $S^{\mathrm{sf}}$). In actual 3-D simulations, the trapezoidal filter $S^{\mathrm{tf}}$ is often applied assuming a ratio of 2 (see, e.g., [33] or [63]). The corresponding value for $S^{\mathrm{sf}}$ based, for instance, on the filter transfer function criterion would be 1.5, as outlined above. All of the specifications mentioned so far have been related to *structured* grids. For the actual *unstructured* version of $S^{\mathrm{tf}}$ expressed in (24) and (25), a ratio of 2 was chosen for the applications in [22].

In the present study, ratios of 2 and 1.5 are applied for $S^{\mathrm{tf}}$ and $S^{\mathrm{sf}}$, respectively. This is in compliance with the choice, at least for $S^{\mathrm{tf}}$, in [22], which is the only of the aforementioned studies applying a discrete smooth filter based on the trapezoidal rule as given in (24) and (25) in an actual 3-D simulation on unstructured grids. The a priori chosen values for the characteristic length-scale ratio will be compared to the estimated values based on the results obtained from the actual simulations.

### 6.3. Comparing the methods

In order to compare the various methods, the scale-separating operator $S^{\mathrm{pm}}$ (i.e., the only projective operator considered in the present study) is used for DS, CMS, and DMS. Figs. 6 and 7 depict the mean

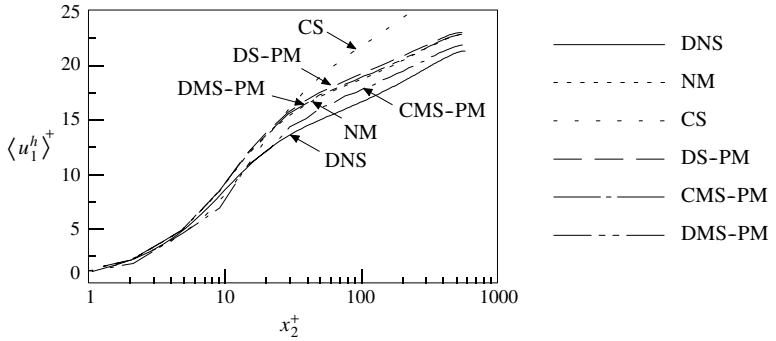


Fig. 6. Mean streamwise velocity for $Re_\tau = 590$: comparing all methods (pm-separation).

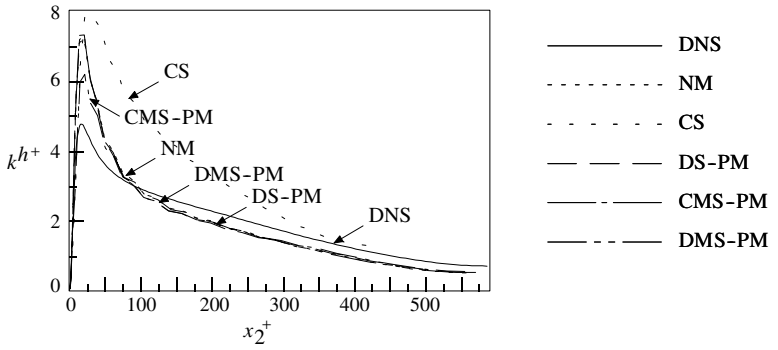


Fig. 7. Turbulent kinetic energy for $Re_\tau = 590$: comparing all methods (pm-separation).

Table 3
$x_2$-integral of the deviation from the DNS profile for the mean streamwise velocity $e_0^u$ and the turbulent kinetic energy $e_0^k$ according to (59) for all methods (pm-separation)

| | Velocity ($Re_\tau = 180$) | Energy ($Re_\tau = 180$) | Velocity ($Re_\tau = 590$) | Energy ($Re_\tau = 590$) |
|---|---|---|---|---|
| NM | 1.52% | 7.69% | 0.87% | 6.68% |
| CS | 9.54% | 90.02% | 6.04% | 78.73% |
| DS-PM | 2.77% | 14.34% | 1.22% | 6.99% |
| CMS-PM | 0.43% | 2.56% | 0.20% | 3.19% |
| DMS-PM | 1.59% | 7.88% | 0.95% | 6.91% |

streamwise velocity profile and the turbulent kinetic energy, respectively, for $Re_\tau = 590$. Table 3 provides a quantitative picture by showing the $x_2$-integral of the deviation from the DNS profile for $Re_\tau = 180$ and $Re_\tau = 590$. A large numerical error introduced by a second-order accurate method in combination with a relatively coarse resolution already mentioned in Section 1 comes into play for all methods. However, the lower accuracy of the basic method affects CMS-PM *to a far lesser extent than the other methods* towards the channel center. It is considerably closer to the DNS profile in this part of the channel than NM, DS-PM, and DMS-PM. This qualitative observation can be quantified by analyzing the $x_2$-integral of the deviation from the DNS profile, see Table 3. CMS-PM is the only one of the investigated methods producing deviations of less than 1% for $Re_\tau = 180$ and less than 0.5% for $Re_\tau = 590$. DMS-PM shows no improvement in comparison to NM, and DS-PM performs even worse. Despite the higher accuracy in the inertial layer (usually expected to start at $x_2^+ = 30$), CMS-PM *underpredicts the velocity profile* in the buffer layer (usually expected to range from $x_2^+ = 5$ to $x_2^+ = 30$). The profile for the turbulent kinetic energy using CMS-PM shows a much better agreement for the height of the peak in comparison to the DNS profile than all other methods. DS-PM shows the worst correspondence to DNS, apart from CS, concerning the peak. These observations can also be quantified by analyzing the $x_2$-integral of the deviation from the DNS profile, see Table 3. CMS-PM yields deviations of about 2.6% for $Re_\tau = 180$ and 3.2% for $Re_\tau = 590$, whereas the next best method (i.e., NM) produces deviations of about 7.7% and 6.7%, respectively. It is emphasized that NM outperforms all modeling approaches but CMS-PM at both Reynolds numbers. This is in accordance with results in [38,56]. For the mean streamwise velocity profiles, which were obtained with a second-order accurate method in those studies, DS was also more or less clearly outperformed by NM at even higher Reynolds numbers $Re_\tau \approx 1000$ and $Re_\tau \approx 1800$.

An objective comparison of the computational effort for the simulations using the aforementioned methods is difficult, since it strongly depends on the number of iterations necessary for the SOR solver to achieve convergence as well as on the amount of computational time spent within the algebraic multigrid

solver. These time measures can vary considerably from one calculation to another. Thus, only approximate measures for the necessary computational effort are reported as a mean value of the actual simulation times covering all calculations of this work as well as additional calculations for finer resolutions in both cases presented in [15]. Setting the computational effort for NM to 1.0, the relative measures for CS, DS-PM, CMS-PM, and DMS-PM are, ca. 1.10, 1.15, 1.10, and 1.15, respectively. Thus, CMS in combination with PM is a very efficient method computationally, even more efficient than DS.

### 6.4. Comparing the scale-separating operators

The second important issue concerns the differences between the various scale-separating operators. In Figs. 8 and 9, the mean streamwise velocity and the turbulent kinetic energy, respectively, for the four scale-separating operators applied with DS, CMS, or DMS are pictured for $Re_\tau = 590$. The $x_2$-integrals of the deviation from the respective DNS profiles for $Re_\tau = 180$ and $Re_\tau = 590$ are given in Table 4. The results for the mean streamwise velocity are almost indistinguishable for DMS, and the ones for the turbulent kinetic energy are also very close, although PM and SM appear to perform slightly better, see Figs. 8 and 9(c).

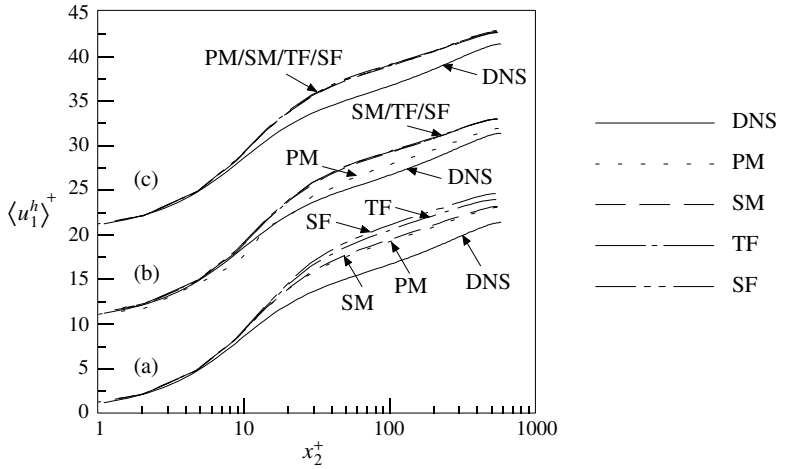


Fig. 8. Mean streamwise velocity for $Re_\tau = 590$: (a) DS; (b) CMS (+10); (c) DMS (+20).

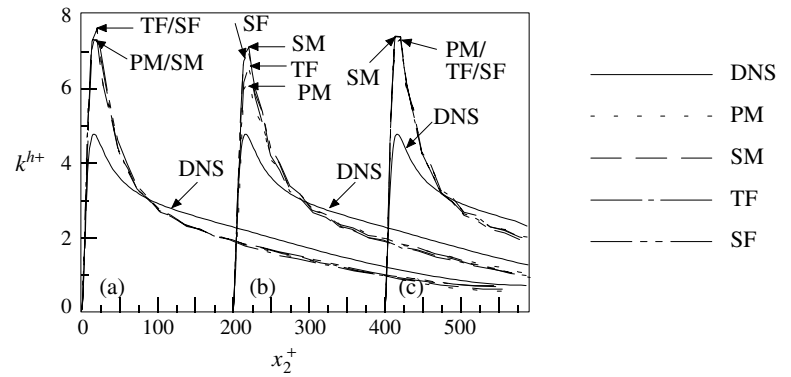


Fig. 9. Turbulent kinetic energy for $Re_\tau = 590$: (a) DS; (b) CMS (+200); (c) DMS (+400).

Table 4
$x_2$-integral of the deviation from the DNS profile for the mean streamwise velocity $e_0^u$ and the turbulent kinetic energy $e_0^k$ according to (59) for all scale-separating operators and methods DS, CMS, and DMS

| | Velocity ($Re_\tau = 180$) | Energy ($Re_\tau = 180$) | Velocity ($Re_\tau = 590$) | Energy ($Re_\tau = 590$) |
|---|---|---|---|---|
| DS-PM | 2.77% | 14.34% | 1.22% | 6.99% |
| DS-SM | 3.30% | 19.03% | 1.41% | 6.58% |
| DS-TF | 5.78% | 42.75% | 2.77% | 7.64% |
| DS-SF | 7.34% | 43.26% | 3.84% | 7.79% |
| CMS-PM | 0.43% | 2.56% | 0.20% | 3.19% |
| CMS-SM | 1.94% | 8.63% | 1.13% | 6.02% |
| CMS-TF | 3.47% | 15.74% | 1.23% | 4.43% |
| CMS-SF | 2.34% | 11.45% | 1.16% | 5.82% |
| DMS-PM | 1.59% | 7.88% | 0.95% | 6.91% |
| DMS-SM | 1.51% | 9.21% | 0.89% | 6.90% |
| DMS-TF | 2.27% | 16.44% | 0.93% | 7.24% |
| DMS-SF | 1.75% | 12.02% | 0.86% | 7.62% |

For DS, better results for PM and SM are already visible for the mean streamwise velocity profile, see Fig. 8(a). They are confirmed by the turbulent kinetic energy profile in Fig. 9(a). Most importantly, a remarkable difference between the projective scale-separating operator PM and the other operators shows up both for the mean streamwise velocity as well as for the turbulent kinetic energy profile in the context of CMS, see Figs. 8 and 9(b). Thus, the favourable behaviour of CMS-PM in the inertial layer as well as the slightly underpredictive performance in the buffer layer and parts of the viscous sublayer seems to be attributed to CMS exclusively depending on this specific scale-separating operator. Analyzing the quantitative results in Table 4, it is apparent that CMS-PM yields the by far smallest deviations from the respective DNS profiles for both the mean streamwise velocity and the turbulent kinetic energy with respect to the flows at both Reynolds numbers.

Specifying the necessary computational effort for the various scale-separating operators results in the following approximate numbers, where the results for the finer resolutions in [15] are also taken into account. Setting the relative computational simulation time for the operator PM to 1.0, the measures for SM, TF, and SF are approximately 1.25, 1.40, and 2.50, respectively. In particular, SF in the current implementation is an extremely time-consuming operator and is, therefore, not recommended for further use. As already mentioned at the end of Section 5, the reason for the additional effort linked with such non-projective operators can be traced back to the call of the scale-separating routine at the beginning of each solver iteration step, in order to determine the updated large-scale velocity field for the residual calculation.

**Remark.** For the simulations with finer resolutions, which are discussed in an extended version of the present study [15], the large numerical error appearing in the results of Sections 6.3 and 6.4 is greatly reduced, and all LES profiles converge to the DNS profile. Therefore, the differences between the various methods and scale-separating operators investigated in Sections 6.3 and 6.4 become less obvious.

### 6.5. Extracting and investigating the small scales

In order to analyze the specific behaviour of CMS-PM in comparison to all other scale-separating operators in the context of CMS, the small scales are extracted and investigated explicitly in this section. Figs. 10 and 11 depict the mean streamwise small-scale velocity and the small-scale turbulent kinetic energy, respectively, for $Re_\tau = 590$. Qualitatively similar results have been obtained for $Re_\tau = 180$, see [15]. The small-scale velocity for CMS-PM shows an oscillating behaviour with large amplitudes, particularly in the buffer

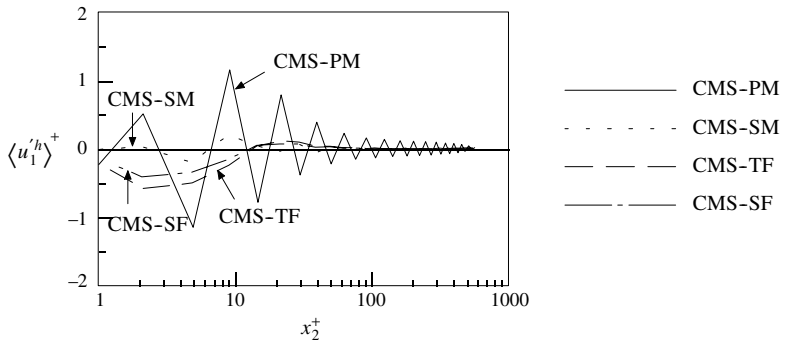


Fig. 10. Mean streamwise small-scale velocity for $Re_\tau = 590$.

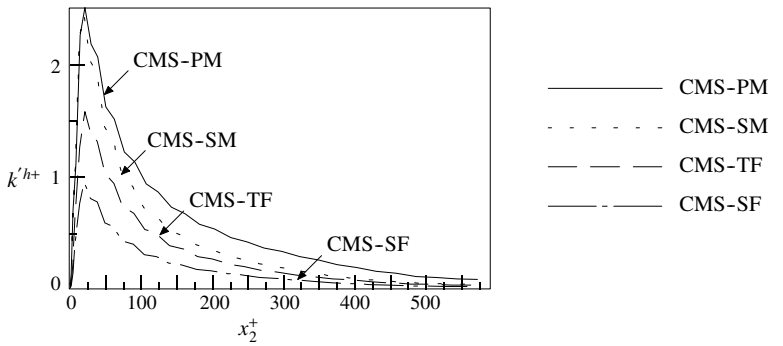


Fig. 11. Small-scale turbulent kinetic energy for $Re_\tau = 590$.

layer. For CMS-SM, the frequency of the oscillation is about the same, but the amplitudes are considerably smaller. In the case of CMS-TF and CMS-SF, one oscillation period can be seen throughout one half-width of the channel, with the amplitude being larger for CMS-TF than for CMS-SF. The largest small-scale turbulent kinetic energy is obtained for CMS-PM and the smallest one for CMS-SF, evaluated by evidence of the $x_2$-*integral* of the small-scale turbulent kinetic energy profiles (i.e., the integral of the curves in Fig. 11). This represents a first measure for the amount of small scales extracted by the respective scale-separating operator and will be quantified in the second part of this section. All of the aforementioned observations are qualitatively confirmed by the results from the finer resolutions in [15].

The second part of this section is devoted to determining an actual value for the characteristic length-scale ratio of the various scale-separating operators with the aid of the results from the CMS simulations. Table 5 contains the results for $Re_\tau = 180$. The analogous data for $Re_\tau = 590$ are contained in Table 6.

Table 5
Characteristic velocity scales and velocity scale ratios for CMS and $Re_\tau = 180$

| | (1): Char. velocity | (2): Char. l. − s. vel. | (3): Char. s. − s. vel. | (4) = (3)/(1) (%) | (5) = 2 × (4)/(4) − SM |
|---|---|---|---|---|---|
| PM | 17.23 | 17.17 | 1.33 | 7.72 | 2.46 |
| SM | 18.31 | 18.27 | 1.15 | 6.28 | 2.00 |
| TF | 19.34 | 19.26 | 1.00 | 5.17 | 1.65 |
| SF | 18.66 | 18.59 | 0.73 | 3.91 | 1.25 |

Table 6
Characteristic velocity scales and velocity scale ratios for CMS and $Re_\tau = 590$

| | (1): Char. velocity | (2): Char. l. − s. vel. | (3): Char. s. − s. vel. | (4) = (3)/(1) (%) | (5) = 2 × (4)/(4) − SM |
|---|---|---|---|---|---|
| PM | 19.66 | 19.63 | 1.08 | 5.49 | 2.54 |
| SM | 20.30 | 20.28 | 0.88 | 4.33 | 2.00 |
| TF | 20.58 | 20.54 | 0.75 | 3.64 | 1.68 |
| SF | 20.37 | 20.34 | 0.57 | 2.80 | 1.29 |

Columns (1)–(3) exhibit the characteristic velocity $u_{\text{char}}$ subject to (60) as well as the large- and small-scale part $\bar{u}_{\text{char}}$ and $u'_{\text{char}}$, respectively. In column (4), the ratio of $u'_{\text{char}}$ to $u_{\text{char}}$ gives a quantitative value for the amount of small scales extracted by the various scale-separating operators. These values are then related to the a priori assumed ratio 2 for SM, in order to obtain characteristic length-scale ratios for the remaining operators relative to this fixed value. The mean ratio for PM in Tables 5 and 6 is 2.5 (i.e., exactly the value chosen a priori). Considering also the finer resolutions in [15], the mean ratio increases to 2.65, but is still fairly close to the chosen value of 2.5. Furthermore, it may be observed that the choice of 2 and 1.5 for TF and SF, respectively, is, at least, a more reasonable one than $\sqrt{6}$ (or even 2.67) and 2. The calculations in the present study, however, suggest even lower values of about 1.7 and 1.3, respectively. It has to be re-emphasized that the preceding quantitative assessment based on the numbers in Tables 5 and 6 has to be considered an *approximate quantification*, see the related discussion in Section 6.2.

### 6.6. Further investigation in an artificial setup

Surprisingly good results for CMS-PM in comparison to the other combinations shown in Sections 6.3 and 6.4 have given rise to an additional investigation. In this examination, the addition of the subgrid viscosity is artificially confined to the buffer layer of the channel. By analyzing the curves obtained for the mean value of the dynamically determined model parameter $\langle C_S \rangle$ in [15], it has been found that the most important difference between CMS and DMS occurs in the region close to the wall, where $\langle C_S \rangle$ is much smaller than the constant value $C_S = 0.1$. Thus, the artificial setup looks as follows. A constant-coefficient-based CMS-PM calculation is conducted, where a constant value for $C_S = 0.1$ is applied only in the buffer layer (i.e., between $x_2^+ = 5$ and $x_2^+ = 30$). Everywhere else in the channel domain, a no-model strategy is pursued. The same is done for the non-multiscale case CS, to provide a direct comparison. Leaving aside the viscous sublayer, this strategy is motivated by the observation that in this particular range a notable difference between the dynamically determined values for $\langle C_S \rangle$ and the a priori chosen constant occurs.

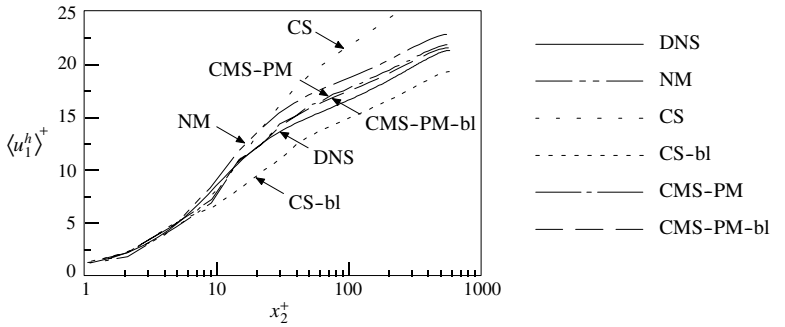


Fig. 12. Mean streamwise velocity for $Re_\tau = 590$: comparing artificial setup.

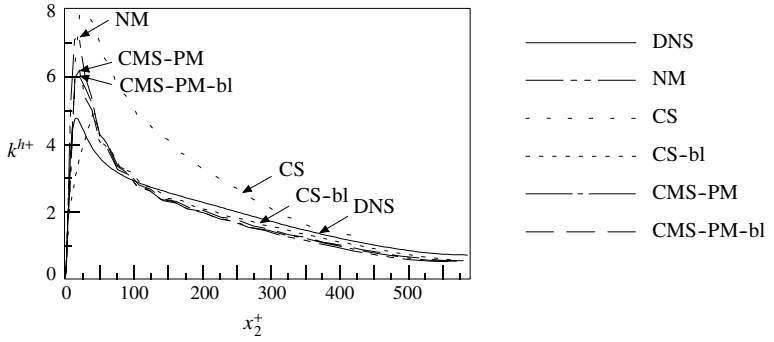


Fig. 13. Turbulent kinetic energy for $Re_\tau = 590$: comparing artificial setup.

The results obtained in this artificial setup are reported in Figs. 12 and 13 for $Re_\tau = 590$, respectively. Qualitatively similar results have been obtained for $Re_\tau = 180$, see [15]. A huge difference for CS is observed, although this now leads from a clear overprediction to a distinct underprediction in the inertial layer, particularly for the higher Reynolds number case. The more important result of this investigation, however, is that the differences between CMS-PM in this artificial setup and in the usual setup are only of very small amount and, thus, insignificant. *This indicates the relative importance of adding a relatively high subgrid viscosity to the small scales in the buffer layer and the relative unimportance of the amount of subgrid viscosity added to the small scales in other parts of the channel for the quality of the results overall.* The situation is completely different, if the addition of subgrid viscosity is not restricted to the small scales (i.e., for CS). In this case, the addition of subgrid viscosity in all parts of the channel has a huge impact on the results in all parts of the channel.

From the *physical* point of view, it is well known that the buffer layer is the site of vigorous turbulence dynamics, with the turbulent energy production rate reaching its maximum within this region (see, e.g., [60]). Overall, a very intense dissipation has to be expected in this region, according to, e.g., analyses of DNS databases in [20]. This may underline the necessity to let a considerably high amount of subgrid viscosity act particularly on the small scales in this region. However, it was shown in [20] that a considerable amount of backscatter can also be observed in this region, especially around $x_2^+ = 12$. It is referred to [20] for elaboration. Note that the actual location strongly depends on the Reynolds number, since $x_2^+ = x_2\ Re_\tau$ for the channel with a half-width of unit length (i.e, the location is closer to the wall for higher Reynolds number). There is no possibility to account for this with a subgrid-viscosity model as it is used in this work, even when it is embedded into the multiscale environment. This might be considered a potential reason why CMS-PM still shows deficient (i.e., underpredictive) results in this region.

A potential *numerical* influence, which also has to be considered in this context, may be traced back to the effect of mesh stretching. This effect has recently been detected for finite difference methods in [30] and for the staggered finite volume method underlying the original CDP code (see [52]) in [2]. Mesh stretching ratios up to about 60 were investigated in [2]. In particular, the upper limit ratio of about 60 was analyzed for various subgrid-scale models. It was shown that the *dynamic* Smagorinsky model is differently influenced within a multiscale and a non-multiscale environment (i.e., DMS and DS). The most important differences to the present investigation can be found in the differences between the original CDP code and the present CDP-$\alpha$ code (i.e., among other things, the switch from a staggered to a colocated variable arrangement for the underlying finite volume method), relatively lower mesh stretching ratios of about 10 and 20 for $Re_\tau = 180$ and $Re_\tau = 590$, respectively, and the particular focus on the *constant-coefficient-based* Smagorinsky model, at least in this additional investigation in an artificial setup, although a different influence of a potential mesh stretching effect on CMS and CS might also be expected.

### 6.7. Summary of observations

The most important observations from the preceding investigations are summarized in the following.

- Different behaviour as a result of using different scale-separating operators can be recognized. This difference is particularly observable in the context of CMS and DS. The use of DMS seems to eliminate differences to a great extent, see Table 4. For instance, the velocity deviation $e_0^{\mathrm{u}}$ for DMS using various scale-separating operators ranges from 1.51% to 2.27% for $Re_\tau = 180$ (i.e., a band of 0.76%) and from 0.86% to 0.95% for $Re_\tau = 590$ (i.e., a band of 0.09%). The respective bands for DS (CMS) are: 3.01% (3.04%) for $Re_\tau = 180$ and 2.62% (1.03%) for $Re_\tau = 590$. It is interesting to note that the differences between the various scale-separating operators diminish with increasing Reynolds number for all methods. For finer resolutions, the aforementioned relative trends among the various methods and scale-separating operators are qualitatively similar, although the absolute values for the velocity and energy deviations become smaller, see [15].
- The scale-separating operator PM plays a specific role in this context due to its projective property, which is not shared by any of the other operators. This specific role is underlined by the results of the numerical simulations, at least in the context of CMS, where the results show the most significant differences to all other methodical combinations.
- The scale-separating operators PM and SM proposed in this work are superior to the discrete smooth filters TF and, particularly, SF as implemented concerning the important issue of computational cost (i.e., a reduction of about 25%, 40%, and 150% for PM compared to SM, TF, and SF, respectively). The use of PM may even reduce the required computational effort for CMS to a value lower than the one for the widely used DS combined with any scale-separating operator (i.e., in particular, a reduction of about 5% for CMS with PM compared to DS with PM). For all other operators (i.e., SM, TF, and SF), the computational effort for CMS is larger than the one for DS.
- Cross-comparison of the methods DS, CMS, and DMS (see Figs. 8 and 9) without specific reference to any of the scale-separating operators reveals better results for the multiscale methods CMS and DMS with respect to DS. The quality of the results ranges from slightly to significantly better, depending on the Reynolds number and the resolution level. For the simulations in the present study, this may be quantified using the results in Table 4. The mean values for $e_0^{\mathrm{u}}$ ($e_{\mathrm{k}}^0$), taking into account all scale-separating operators, are 4.80% (29.85%), 2.05% (9.60%), and 1.78% (11.39%) for DS, CMS, and DMS, respectively, for $Re_\tau = 180$. For $Re_\tau = 590$, the respective mean values for DS, CMS, and DMS are 2.31% (7.25%), 0.93% (4.87%), and 0.91% (7.17%). With the resolution being refined, the results for the various methods converge, see the respective results in [15].
- Surprisingly, the apparently more sophisticated and more costly dynamic method DMS shows no better, or even worse results than the simple constant-coefficient-based method CMS. This indicates that the dynamic modeling procedure does not appropriately determine the model parameter in the context of the variational multiscale LES.
- Even for the classical dynamic model procedure DS, the use of the scale-separating operators PM and SM proposed in this work seems to be more favourable in comparison to the classical discrete smooth filters TF and SF, both from the standpoint of quality of results as well as computational cost.
- The no-model approach (NM) outperforms all methodical combinations but CMS-PM within the present numerical setup. This confirms results in [38,56] and raises doubts about the usefulness of all those subgrid-scale modeling approaches within a second-order accurate numerical method, except for the particular combination CMS-PM.
- Characteristic length-scale ratios for the various scale-separating operators can be (at least) approximately estimated from the results.

- The importance of introducing a substantial amount of subgrid viscosity to the small scales, particularly in the buffer layer of the channel, is pointed out. A still existing potential deficiency of the variational multiscale LES due to the inability to account for backscatter with the models chosen in this work is also pointed out.

## 7. Conclusions

A general class of scale-separating operators based on combined multigrid operators has been proposed and analyzed in this work. Two operators of this class have been compared to widely used discrete smooth filters, and essential differences have been pointed out. In particular, it has been shown that the scale-separating operators are not only theoretically different, but also yield considerable differences in the respective numerical results for the problem simulated. All operators are suited for variational multiscale LES, both with dynamic and constant-coefficient-based subgrid-scale modeling. They may also be used for the dynamic modeling procedure in a classical LES. Only one of the scale-separating operators proposed, however, exhibits the important idempotence property of a projector, allowing fulfillment of the theoretical assumption for a clear scale separation within the variational multiscale method.

All of the scale-separating operators have been implemented in a second-order accurate, energy-conserving finite volume method particularly suited for incompressible Navier–Stokes flow applications on hybrid unstructured grids in complex geometries. Dynamic and non-dynamic subgrid-scale modeling methods based on the various scale-separating operators have been tested for the case of a turbulent channel flow with relatively coarse resolutions at two different Reynolds numbers. Several important observations have been made and summarized in the preceding section. With respect to certain crucial flow features, the simple constant-coefficient Smagorinsky-model based variational multiscale method in combination with the projective operator has shown remarkable results. In particular, it has proven to be a very efficient combination with regard to the important aspect of computational cost, resulting in a reduction in computing time ranging from about 25% up to about 150% compared to the other operators. The introduction of a substantial amount of subgrid viscosity to the small scales, particularly in the buffer layer of the channel, appears to be crucial for the good results achieved with this method. A potential deficiency may still be found in the impossibility to account for backscatter with the subgrid viscosity concept, even within the multiscale environment. More sophisticated subgrid-scale models which take backscatter into account may lead to additional improvement. It is intended to investigate the performance of the scale-separating operators based on combined multigrid operators in the context of the methods used in this work on further flow problems in subsequent studies.

## Acknowledgements

The author's postdoctoral research stay at the Center for Turbulence Research, during which this work originated, was supported by a Feodor Lynen Research Fellowship of the Alexander of Humboldt-Foundation, jointly funded by the Center for Turbulence Research and the Alexander von Humboldt-Foundation. This support is gratefully acknowledged. The author would like to express his sincere appreciation to Frank Ham for providing a basic version of the CDP-$\alpha$ code for the simulation of incompressible flows, which the developments of this work are built upon. The author is also grateful to Parviz Moin and Greg Burton for helpful discussions.

## References


[1] G.-P. Bonneau, Multiresolution analysis on irregular surface meshes, IEEE Trans. Visual. Comp. Graph. 4 (1998) 365–378.
[2] V.M. Calo, Residual-based multiscale turbulence modeling: finite volume simulations of bypass transition, PhD Thesis, Department of Civil and Environmental Engineering, Stanford University, 2004. Available from: <http://www.ices.utexas.edu/~victor/vmc-thesis.pdf>.
[3] H. Choi, P. Moin, Effects of the computational time step on numerical solutions of turbulent flow, J. Comput. Phys. 113 (1994) 1–4.
[4] S.S. Collis, Monitoring unresolved scales in multiscale turbulence modeling, Phys. Fluids 13 (2001) 1800–1806.
[5] S.S. Collis, Discontinuous Galerkin methods for turbulence simulation, in: Proceedings of the Summer Program 2002, Stanford University and NASA Ames Research Center, Center for Turbulence Research, 2002, pp. 155–167.
[6] I. Daubechies, Ten lectures on waveletsCBMS-NSF Regional Conference Series in Applied Mathematics No.61, SIAM, Philadelphia, 1992.
[7] I. Daubechies, I. Guskov, P. Schröder, W. Sweldens, Wavelets on irregular point sets, Philos. Trans. R. Soc. Lond. A 357 (1999) 2397–2413.
[8] J.W. Deardorff, A numerical study of three-dimensional turbulent channel flow at large Reynolds numbers, J. Fluid Mech. 41 (1970) 453–465.
[9] T. Dubois, F. Jauberteau, R. Temam, Dynamic Multilevel Methods and the Numerical Simulation of Turbulence, Cambridge University Press, Cambridge, 1999.
[10] J.H. Ferziger, M. Peric, Computational Methods for Fluid Dynamics, second ed., Springer, Berlin, 1999.
[11] M. Germano, Turbulence: the filtering approach, J. Fluid Mech. 238 (1992) 325–336.
[12] M. Germano, U. Piomelli, P. Moin, W.H. Cabot, A dynamic subgrid-scale eddy viscosity model, Phys. Fluids A 3 (1991) 1760–1765.
[13] S. Ghosal, P. Moin, The basic equations for the large-eddy simulation of turbulent flows in complex geometry, J. Comput. Phys. 118 (1995) 24–37.
[14] V. Gravemeier, The variational multiscale method for laminar and turbulent incompressible flow, Ph.D. Thesis, Report No. 40, Institute of Structural Mechanics, University of Stuttgart, 2003. Available from: <http://www.uni-stuttgart.de/ibs/publications/phd/2000/fulltext/phdgravem.pdf>.
[15] V. Gravemeier, Scale-separating operators for variational multiscale large eddy simulation of turbulent flows, CTR Manuscript 187, Center for Turbulence Research, Stanford University and NASA Ames Research Center, 2004.
[16] V. Gravemeier, W.A. Wall, E. Ramm, A three-level finite element method for the instationary incompressible Navier–Stokes equations, Comput. Methods Appl. Mech. Engrg. 193 (2004) 1323–1366.
[17] V. Gravemeier, W.A. Wall, E. Ramm, Large eddy simulation of turbulent incompressible flows by a three-level finite element method, Int. J. Numer. Meth. Fluids 48 (2005) 1067–1099.
[18] F. Ham, S. Apte, G. Iaccarino, X. Wu, M. Herrmann, G. Constantinescu, K. Mahesh, P. Moin, Unstructured LES of reacting multiphase flows in realistic gas turbine combustors, in: Annual Research Briefs – 2003, Center for Turbulence Research, Stanford University and NASA Ames Research Center, 2003, pp. 139–160.
[19] F. Ham, G. Iaccarino, Energy conservation in collocated discretization schemes on unstructured meshes, in: Annual Research Briefs – 2004, Center for Turbulence Research, Stanford University and NASA Ames Research Center, 2004, pp. 3–14.
[20] C. Härtel, L. Kleiser, F. Unger, R. Friedrich, Subgrid-scale energy transfer in the near-wall region of turbulent flows, Phys. Fluids 6 (1994) 3130–3143.
[21] A. Haselbacher, O. Vasilyev, Commutative discrete filtering on unstructured grids based on least-squares techniques, J. Comput. Phys. 187 (2003) 197–211.
[22] D.C. Haworth, K. Jansen, Large-eddy simulation on unstructured deforming meshes: towards reciprocating IC engines, Comput. Fluids 29 (2000) 493–524.
[23] J. Holmen, T.J.R. Hughes, A.A. Oberai, G.N. Wells, Sensitivity of the scale partition for variational multiscale large-eddy simulation of channel flow, Phys. Fluids 16 (2004) 824–827.
[24] T.J.R. Hughes, Multiscale phenomena: Green's functions, the Dirichlet-to-Neumann formulation, subgrid scale models, bubbles and the origins of stabilized methods, Comput. Methods Appl. Mech. Engrg. 127 (1995) 387–401.
[25] T.J.R. Hughes, G.R. Feijoo, L. Mazzei, J.-B. Quincy, The variational multiscale method – a paradigm for computational mechanics, Comput. Methods Appl. Mech. Engrg. 166 (1998) 3–24.
[26] T.J.R. Hughes, L. Mazzei, K.E. Jansen, Large eddy simulation and the variational multiscale method, Comput. Vis. Sci. 3 (2000) 47–59.
[27] T.J.R. Hughes, L. Mazzei, A.A. Oberai, A.A. Wray, The multiscale formulation of large eddy simulation: decay of homogeneous isotropic turbulence, Phys. Fluids 13 (2001) 505–512.
[28] T.J.R. Hughes, A.A. Oberai, L. Mazzei, Large eddy simulation of turbulent channel flows by the variational multiscale method, Phys. Fluids 13 (2001) 1784–1799.

[29] S.R. Idelsohn, E. Onate, Finite volumes and finite elements: two 'good friends', Int. J. Numer. Meth. Engrg. 37 (1994) 3323–3341.
[30] T. Ikeda, P.A. Durbin, Mesh stretch effects on convection in flow simulations, J. Comput. Phys. 199 (2004) 110–125.
[31] K.E. Jansen, A stabilized finite element method for computing turbulence, Comput. Methods Appl. Mech. Engrg. 174 (1999) 299–317.
[32] K.E. Jansen, A.E. Tejada-Martinez, An evaluation of the variational multiscale model for large-eddy simulation while using a hierarchical basis, AIAA Paper 2002-0283, Reno, NV, January 14–17, 2002.
[33] H. Jeanmart, G.S. Winckelmans, Comparison of recent dynamic subgrid-scale models in turbulent channel flow, in: Proceedings of the Summer Program 2002, Center for Turbulence Research, Stanford University and NASA Ames Research Center, 2002, pp. 105–116.
[34] V. John, S. Kaya, A finite element variational multiscale method for the Navier–Stokes equations, SIAM J. Sci. Comp. 26 (2005) 1485–1503.
[35] D. Kim, H. Choi, A second-order time-accurate finite volume method for unsteady incompressible flow on hybrid unstructured grids, J. Comput. Phys. 162 (2000) 411–428.
[36] B. Knaepen, D. Carati, Large-eddy simulation without filter, J. Comput. Phys. 205 (2005) 98–107.
[37] B. Koobus, C. Farhat, A variational multiscale method for the large eddy simulation of compressible turbulent flows on unstructured meshes – application to vortex shedding, Comput. Methods Appl. Mech. Engrg. 193 (2004) 1367–1383.
[38] A.G. Kravchenko, P. Moin, On the effect of numerical errors in large eddy simulations of turbulent flows, J. Comput. Phys. 131 (1997) 310–322.
[39] A. Leonard, Energy cascade in large eddy simulation of turbulent fluid flow, Adv. Geophys. 18A (1974) 237–248.
[40] D.K. Lilly, A proposed modification of the Germano subgrid-scale closure method, Phys. Fluids A 4 (1992) 633–635.
[41] T.S. Lund, On the use of discrete filters for large eddy simulation, in: Annual Research Briefs – 1997, Center for Turbulence Research, Stanford University and NASA Ames Research Center, 1997, pp. 83–95.
[42] K. Mahesh, G. Constantinescu, S. Apte, G. Iaccarino, F. Ham, P. Moin, Progress toward large-eddy simulation of turbulent reacting and non-reacting flows in complex geometries, in: Annual Research Briefs – 2002, Center for Turbulence Research, Stanford University and NASA Ames Research Center, 2002, pp. 115–142.
[43] K. Mahesh, G. Constantinescu, P. Moin, A numerical method for large-eddy simulation in complex geometries, J. Comput. Phys. 197 (2004) 215–240.
[44] A.L. Marsden, O. Vasilyev, P. Moin, Construction of commutative filters for LES on unstructured meshes, J. Comput. Phys. 175 (2002) 584–603.
[45] D.J. Mavriplis, Adaptive meshing techniques for viscous flow calculations on mixed element unstructured meshes, ICASE-Report 97-20, NASA Langley Research Center, Hampton, VA, 1997.
[46] P. Moin, Advances in large eddy simulation methodology for complex flows, Int. J. Heat Fluid Flow 23 (2002) 710–720.
[47] P. Moin, K. Mahesh, Direct numerical simulation: a tool in turbulence research, Ann. Rev. Fluid Mech. 30 (1998) 539–578.
[48] R.D. Moser, J. Kim, N.N. Mansour, Direct numerical simulation of turbulent channel flow up to $Re_\tau = 590$, Phys. Fluids 11 (1999) 943–945.
[49] J.S. Mullen, P.F. Fischer, Filtering techniques for complex geometry fluid flows, Comm. Numer. Meth. Engrg. 15 (1999) 9–18.
[50] A.A. Oberai, T.J.R. Hughes, The variational multiscale formulation of LES: channel flow at $Re_\tau = 590$, AIAA Paper 2002-1056, Reno, NV, January 14–17, 2002.
[51] A.A. Oberai, J. Wanderer, A dynamic approach for evaluating parameters in a numerical method, Int. J. Numer. Meth. Engrg. 62 (2005) 50–71.
[52] C.D. Pierce, P. Moin, Progress-variable approach for large eddy simulation of turbulent combustion, Technical Report TF-80, Department of Mechanical Engineering, Flow Physics and Computation Division, Stanford University, 2001. Available from: <http://ctr.stanford.edu/Pierce/thesis.pdf>.
[53] R.S. Rogallo, P. Moin, Numerical simulation of turbulent flows, Ann. Rev. Fluid Mech. 16 (1984) 99–137.
[54] P. Sagaut, Large Eddy Simulation for Incompressible Flows, second ed., Springer, Berlin, 2002.
[55] P. Sagaut, R. Grohens, Discrete filters for large eddy simulation, Int. J. Numer. Meth. Fluids 31 (1999) 1195–1220.
[56] K.B. Shah, J.H. Ferziger, A new non-eddy viscosity subgrid-scale model and its application to channel flow, in: Annual Research Briefs – 1995, Center for Turbulence Research, Stanford University and NASA Ames Research Center, 1995, pp. 73–90.
[57] J. Smagorinsky, General circulation experiments with the primitive equations. I. The basic experiment, Mon. Weather Rev. 91 (1963) 99–164.
[58] A.E. Tejada-Martinez, K.E. Jansen, Spatial test filters for dynamic model large eddy simulation with finite elements, Comm. Numer. Meth. Engrg. 19 (2003) 205–213.
[59] A.E. Tejada-Martinez, K.E. Jansen, A dynamic Smagorinsky model with dynamic determination of the filter width ratio, Phys. Fluids 16 (2004) 2514–2528.
[60] H. Tennekes, J.L. Lumley, A First Course in Turbulence, MIT Press, Cambridge, MA, 1972.
[61] M. Terracol, P. Sagaut, C. Basdevant, A multilevel algorithm for large-eddy simulation of turbulent compressible flows, J. Comput. Phys. 167 (2001) 439–474.

[62] O. Vasilyev, T.S. Lund, P. Moin, A general class of commutative filters for LES in complex geometries, J. Comput. Phys. 146 (1998) 82–104.
[63] A.W. Vreman, The filtering analog of the variational multiscale method in large-eddy simulation, Phys. Fluids 15 (2003) L61–L64.
[64] A.W. Vreman, The adjoint filter operator in large-eddy simulation of turbulent flow, Phys. Fluids 16 (6) (2004) 2012–2022.
[65] P. Wesseling, An Introduction to Multigrid Methods, Wiley, Chichester, 1992.
[66] C.H. Whiting, K.E. Jansen, A stabilized finite element method for the incompressible Navier–Stokes equations using a hierarchical basis, Int. J. Numer. Meth. Fluids 35 (2001) 93–116.
[67] G.S. Winckelmans, H. Jeanmart, D. Carati, On the comparison of turbulence intensities from large-eddy simulation with those from experiment or direct numerical simulation, Phys. Fluids 14 (2002) 1809–1811.